TNF-α induces type I IFN signalling to suppress neurogenesis and recruit T cells

Tinne Amalie Damgaard Nissen[1,2], Arishma Baig[1], Daniel T. Rock[2], Sandra Shibu[2], Hyunah Lee[2], Lauren A. O'Neill[1], Susan John[3], Linda S. Klavinskis[1]*, Sandrine Thuret[2]*

[1] Department of Infectious Diseases, School of Immunology & Microbial Sciences, King's College London, London SE1 9RT, UK

[2] Department of Basic and Clinical Neuroscience, Institute of Psychiatry, Psychology and Neuroscience, King's College London, London SE5 9RT, UK

[3] Peter Gorer Department of Immunobiology, King's College London, London SE1 9RT, UK

*Equally contributed and co-corresponding authors. Linda.Klavinskis@kcl.ac.uk and Sandrine.1.thuret@kcl.ac.uk

Abstract

Adult hippocampal neurogenesis (AHN) is essential for learning, memory, and mood regulation, and its disruption is implicated in ageing, neurodegeneration, and mood disorders. However, the mechanisms linking inflammation to AHN impairment remain unclear. Here, we identify chronic tumour necrosis factor-alpha (TNF-α) signalling as a key driver of neurogenic dysregulation via a previously unrecognised type I interferon (IFN) autocrine/paracrine loop in human hippocampal progenitor cells (HPCs). Using a human *in vitro* neurogenesis model, single-cell RNA sequencing, and functional T cell migration assays, we show that TNF-α induces a robust type I IFN response in HPCs,

promoting chemokine-mediated, and CXCR3-dependent T cell recruitment and suppressing neurogenesis. This inflammatory signalling cascade drives a fate switch in HPCs from a neurogenic trajectory towards an immune-defensive phenotype, with critical implications for infectious and inflammatory disease pathogenesis. These findings uncover a key inflammatory checkpoint regulating human AHN and highlight potential therapeutic targets to restore neurogenesis in chronic inflammatory states.

Introduction

Adult neurogenesis occurs in two main neurogenic niches in the mammalian brain: the subventricular zone (SVZ) lining the lateral ventricles and the subgranular zone (SGZ) of the dentate gyrus of the hippocampus[1]. Upon activation, hippocampal neural stem cells (NSCs) known as radial glia-like cells (RGLs) divide and differentiate into astrocytes or excitatory, granule cells, integrating into the granule cell layer (GCL). Initially discovered in rodents[2], human adult hippocampal neurogenesis (AHN) has since been demonstrated using carbon dating[3], postmortem tissue[4–7], *in vitro* propagation of adult neural progenitor cells (NPCs)[8], single nucleus RNA sequencing[9], and spatial transcriptomics[10]. AHN in rodents enhances several cognitive functions, including memory and learning[11], the development of individuality[12], and mood regulation[13].

Perturbations in AHN observed in ageing, neurodegenerative diseases, and mood disorders are thought to contribute to cognitive decline and associated symptoms, given AHN's role in memory and mood regulation[14,15]. Experimental enhancement of AHN reduces depressive-like behaviours[16] and rescues memory and emotional deficits in Alzheimer's disease (AD) mice[17]. Emerging evidence suggests that inflammation,

50 elevated in AD[18], ageing[19], and in some individuals with mood disorders such as
51 depression[20], may underlie these AHN deficits. In particular, the proinflammatory cytokine
52 TNF-α has been implicated in both AD[21,22] and depression[23,24], and is known to negatively
53 regulate AHN[25,26]. These observations support a model in which inflammation-driven
54 suppression of AHN contributes to shared clinical phenotypes across disorders. Targeting
55 this axis may represent a viable neuroprotective strategy[15]. Defining the molecular
56 mechanisms by which inflammatory mediators, such as TNF-α, influence hippocampal
57 neural stem cell (NSC) fate is crucial for developing interventions preserving AHN and its
58 associated cognitive functions in inflammatory conditions.

59 Chronic TNF-α-mediated inflammation was recently shown to drive a functional switch in
60 rodent olfactory NSCs, redirecting them from neuroregeneration toward immune
61 recruitment[27]. These NSCs actively recruited inflammatory cells, including T cells, at the
62 expense of their neurogenic capacity. We hypothesised that a similar switch could occur
63 in human hippocampal progenitor cells (HPCs), contributing to impaired AHN and T cell
64 infiltration observed in ageing and neurodegenerative disease, where TNF-α levels are
65 persistently elevated[28–30]. Using an established *in vitro* model of human hippocampal
66 neurogenesis[31–36], we found that chronic TNF-α exposure suppressed neurogenesis and
67 induced robust CXCL10 secretion. Single-cell RNA (scRNA) sequencing revealed that
68 TNF-α activated type I IFN signalling via autocrine/paracrine signalling, a mechanism not
69 previously described in central nervous system (CNS)-resident cells. This signalling
70 cascade drove the secretion of chemokines that mediated CXCR3-dependent T cell
71 chemotaxis and contributed to the anti-neurogenic effects of chronic TNF-α. Together,
72 our findings support a model in which chronic TNF-α reprograms human HPCs from a

73 neurogenic to a proinflammatory state, orchestrated by TNF-α-induced type I IFN
74 signalling.

75 Results

76 TNF-α-driven functional and phenotypic reprogramming of HPCs

77 To investigate how TNF-α reprograms human HPCs, we first confirmed that our cellular
78 model expressed the TNF-α receptors TNFR1 and TNFR2 (Supplementary Fig. 1). TNF-
79 α stimulation of HPCs induced rapid nuclear translocation of NF-κB p65, peaking at 30
80 minutes and remaining elevated for up to 48 hours (Fig. 1a–b), consistent with sustained
81 activation of a canonical proinflammatory pathway implicated in the regulation of
82 neurogenesis[37]. To assess the functional relevance of TNF-α signalling in HPCs and their
83 progeny, we evaluated the secretion of the NF-κB-regulated cytokine IL-6 and a panel of
84 NF-κB-regulated chemokines. Levels were measured in the supernatant at 24 and 48
85 hours after TNF-α treatment of the HPCs, as well as 24 hours, 48 hours, and seven days
86 of TNF-α treatment in differentiating HPCs (Supplementary Fig. 2). Among the
87 chemokines analysed (Supplementary Fig. 3-5), CXCL10 exhibited the most robust
88 induction in response to TNF-α stimulation (Fig. 1c–d). To examine the effects of chronic
89 TNF-α on neuronal differentiation, HPCs were pre-treated ± TNF-α under proliferative
90 conditions for 48 hours, followed by seven days of differentiation with continued TNF-α
91 exposure every 48 hours (Fig. 1e). TNF-α dose-dependently reduced the proportion of
92 doublecortin (DCX)+ neuroblasts (Fig. 1g), while only the highest dose (10 ng/ml)
93 decreased the percentage of cells expressing the neuronal marker microtubule-
94 associated protein 2 (MAP2) (Fig. 1h). In parallel, TNF-α reduced total neurite length in
95 both populations, indicating impaired morphological maturation (Supplementary Fig. 6).

Collectively, these findings suggest that chronic TNF-α functionally and phenotypically reprograms HPCs.

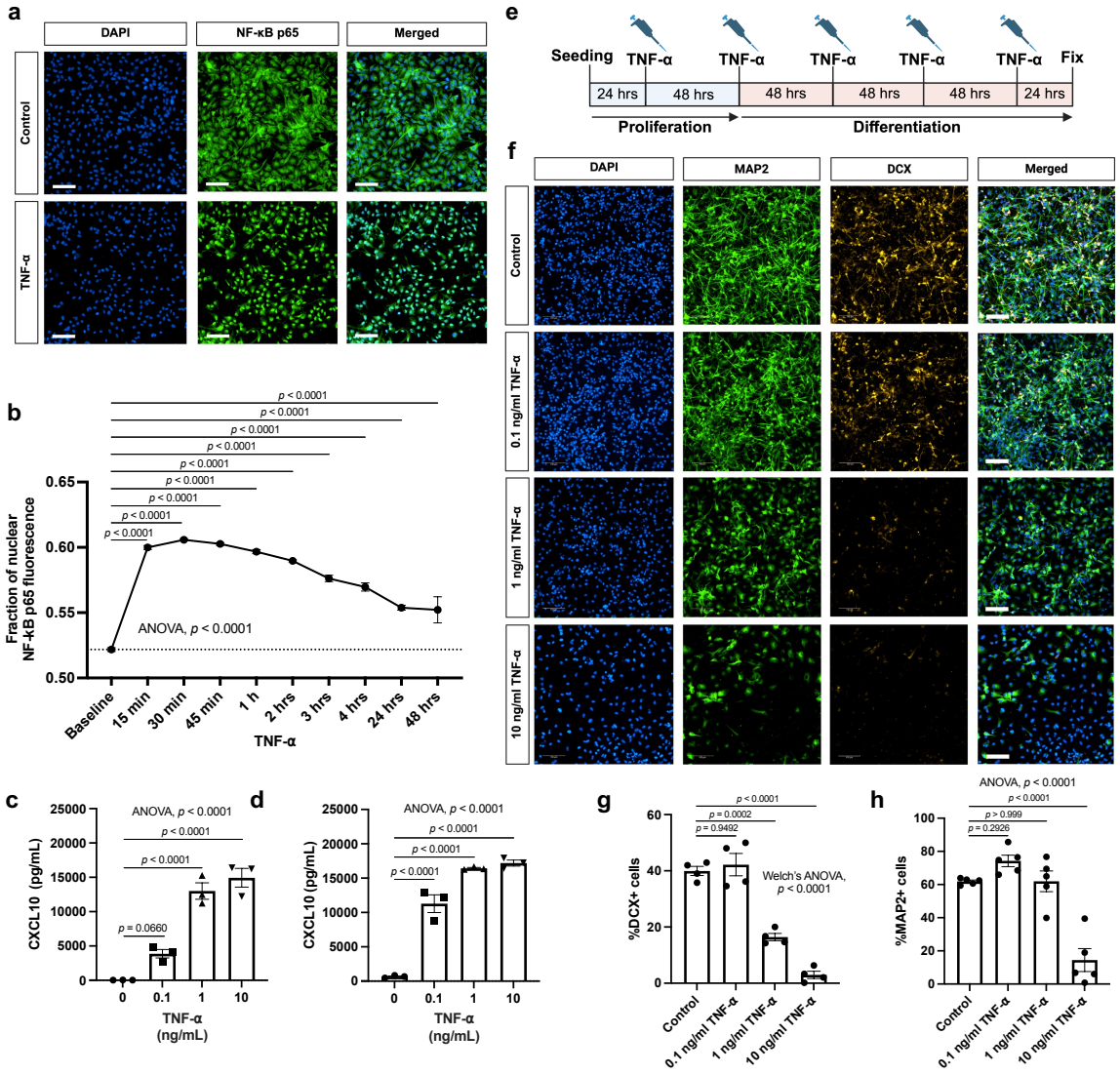

Fig. 1 | TNF-α drives immune signalling and decreases neurogenesis in human hippocampal progenitor cells. a, Representative immunocytochemistry images of three independent experiments with similar results showing the expression of NF-κB p65 on HPCs treated ± 10 ng/ml TNF-α for 15 minutes. Scale bar represents 100 μm. **b**, Quantification of the fraction of nuclear NF-κB p65 fluorescence intensity relative to total cellular fluorescence. Data represent mean ± SEM from n = 3. Statistical analysis: one-way ANOVA followed by Bonferroni multiple comparisons test. **c**, and **d**, Quantification of CXCL10 levels in culture supernatants measured by ELISA. **c**, HPCs under proliferation conditions treated for 48 hours ± 0.1, 1, or 10 ng/ml TNF-α. **d**, HPCs under differentiation conditions treated for 7 days ± 0.1, 1, or 10 ng/ml TNF-α. Data represent mean ± SEM from n = 3. Statistical analysis: one-way ANOVA followed by Bonferroni

multiple comparisons test. **e**, Schematic overview of the chronic TNF-α treatment regime for investigating its effect on neuronal differentiation. HPCs were treated under proliferation conditions for 48 hours ± 0.1, 1, or 10 ng/ml TNF-α before inducing differentiation for seven days under treatment ± 0.1, 1, or 10 ng/ml TNF-α every 48 hours. **f**, Representative images showing the expression of MAP2 (green) and DCX (orange) on seven days differentiated HPCs treated chronically ± 0.1, 1, or 10 ng/ml TNF-α. Scale bar represents 100 µm. **g**, and **h**, Quantification of the percentage of DCX+ cells and MAP2+ cells respectively based on **f**. Data represent mean ± SEM from. **g**, Data based on *n* = 4. Statistical analysis: Welch's ANOVA followed by Games-Howell post-hoc test for pairwise comparisons. **h**, Data based on *n* = 5. Statistical analysis: one-way ANOVA followed by Bonferroni multiple comparisons test.

Chronic TNF-α disrupts neuronal differentiation and upregulates a transcriptional type I IFN signature

To elucidate the molecular mechanisms underlying the effects of chronic TNF-α, we performed scRNA sequencing of HPCs exposed for 48 hours to low (0.1 ng/ml) or high (1 ng/ml) TNF-α, as well as their progeny after 7 and 14 days of differentiation under chronic TNF-α exposure (Fig. 2a). After quality control, 22,133 cells were identified across 15 clusters, including astrocyte-like (clusters 1-4), radial glial-like (RGL)/NSC-like (5-6), intermediate progenitor cell (IPC)-like (7-10), neuroblast-like (11), and immature neuron-like (12) clusters (Fig. 2b-d). The neurogenic identity of clusters 11 and 12 was confirmed by overlap with a human immature granule cell signature[9] and by enrichment of neuronal biological processes and cellular compartment gene ontology (GO) terms (Fig. 2e-g and Supplementary Fig. 7). Critically, HPCs differentiated in the presence of high-dose TNF-α showed a marked reduction in cells within neurogenic clusters (Fig. 2h), demonstrating disrupted neurogenesis.

While control and low-dose TNF-α treated cells clustered together, high-dose TNF-α treated cells formed distinct clusters (Extended Fig. 1a). RGL-like cluster 6 and IPC-like

134 cluster 10, primarily composed of HPCs treated with high-dose TNF-α, exhibited strong
135 upregulation of type I interferon (IFN) response genes including *ISG15*, *IFI27*, and *IFI6*
136 (Fig. 3a-b). GO enrichment analysis highlighting "response to type I IFNs" and phagocytic
137 vesicle components (Extended Fig. 1c-d; Supplementary Fig. 8). The type I IFN signature
138 was detected across clusters specific to treatment with high-dose TNF-α (Fig. 3c). HPCs
139 differentiated with high-dose TNF-α failed to align with astrocyte-, neuroblast-, or
140 immature neuron-like clusters, indicating disrupted lineage commitment and
141 transcriptional dysregulation. Go term analysis of clusters 13-15 indicated a shift toward
142 aberrant, immune-reactive states with activation of a type I IFN-mediated antiviral
143 program (Fig. 3d-f). Given that TNF-α does not directly induce type I IFN response genes,
144 we hypothesised that a type I IFN autocrine/paracrine loop mediated the ISG
145 upregulation. HPCs and their progeny expressed the machinery to respond to type I IFNs
146 (Supplementary Fig. 9), and cells from high-dose TNF-α-specific clusters strongly
147 overlapped with an NSC-specific IFN-β response signature[38] (Fig. 3g). Transcription
148 factor activity analysis predicted STAT1, STAT2, and IRF9 activity in these clusters,
149 consistent with IFN signalling (Fig. 3h). Together, these findings demonstrate that chronic
150 TNF-α exposure induces type I IFN response genes in HPCs, suppresses neurogenesis,
151 and promotes aberrant immune-reactive cellular states during differentiation.

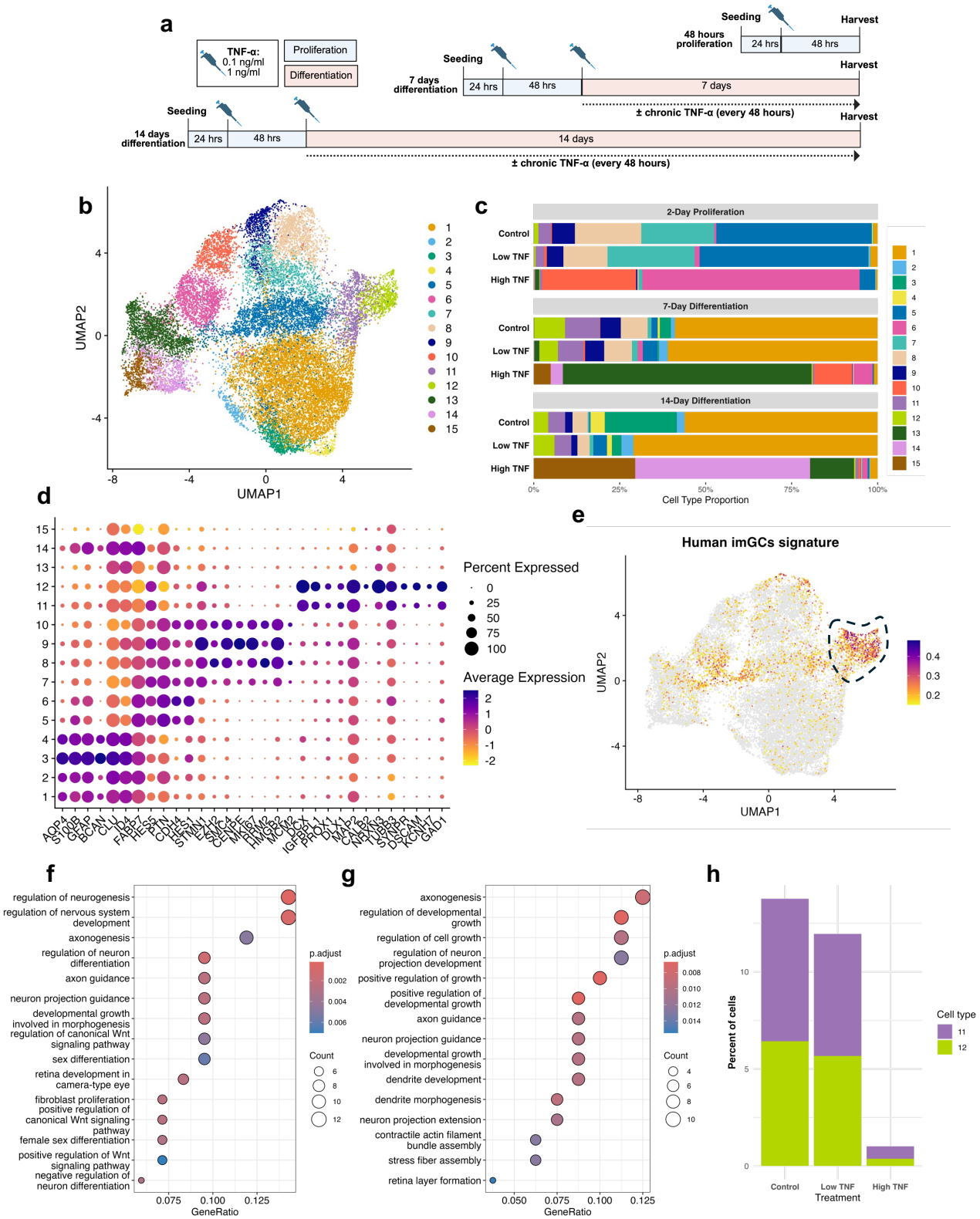

Fig. 2 | Chronic TNF-α impairs neuronal differentiation. a, Schematic overview of the experimental design. **b**, UMAP plot showing transcriptional clustering of single cells. Colors indicate the 15 cell clusters

identified. **c**, Stacked bar graphs showing the frequencies of cell clusters shown in **b** across the time and treatment groups. **d**, Dot plot showing the expression of canonical marker genes for expected cell types across the cell clusters. **e**, UMAP plot showing each cell scored against a human immature granule cells (imGCs) signature[9]. The outlined area highlight the of the signature with cluster 11 and 12. **f**, and **g**, dot plots showing GO enrichment analysis of biological process terms based on the top 100 genes positively defining cluster 11 and cluster 12 respectively. **h**, Bar plots show the percentage cells belonging to the neurogenic cluster 11 (green) and 12 (purple) within differentiation samples from 7 and 14 days by treatment condition: control, low TNF (0.1 ng/ml), and high TNF (1 ng/ml).

TNF-α drives type I IFN signalling through activation of IFNAR

As STAT1 negatively regulates human hippocampal neurogenesis[39] and STAT1/STAT2 regulates the expression of type I IFN-regulated genes, we assessed their activation in HPCs following TNFa stimulation. Phosphorylation of both STAT1 and STAT2 was delayed, peaking at 3–6 hours (STAT1: Fig. 4a–b and Supplementary Fig. 11; STAT2: Extended Fig. 2a–b and Supplementary Fig. 12; GAPDH stability in response to TNF-α: Supplementrary Fig. 10), consistent with a mechanism of indirect activation. In line with an autocrine/paracrine loop, factors secreted downstream of TNF-α-mediated receptor engagement increased the percentage of ISG15+ HPCs (Extended Fig. 2c–d). TNF-α transiently induced *IFNB1* expression, peaking at 3 hours (Fig. 4b), temporally correlating with STAT1/STAT2 activation, suggesting IFN-β as the likely mediator. TNF-α-induced *IFNB1* expression depended on NF-κB signalling (Extended Fig. 2e) but was independent of *de novo* protein synthesis (Extended Fig. 2f). As IRF1 is required for TNF-α–induced *IFNB1* expression in other cell types[40,41], we examined its regulation in HPCs. TNF-α markedly upregulated *IRF1*, peaking at 3 hours (Supplementary Fig. 13), preceding *IFNB1* induction and suggesting a potential regulatory role for IRF1 in HPC *IFNB1* induction. TNF-α-induced upregulation of the STAT1/STAT2-regulated chemokine CXCL10 has been found to depend on IFN-β[42]. Consistent with this, the delayed induction

181 of *CXCL10* in response to TNF-α in HPCs required *de novo* protein synthesis, as shown
182 by its sensitivity to cycloheximide treatment (Fig. 4d-e). To confirm that TNF-α induces
183 type I IFN signalling via an autocrine/paracrine loop, we blocked the IFN-α/β receptor
184 (IFNAR) using the antibody anifrolumab[43]. Anifrolumab fully abolished TNF-α-induced
185 STAT1+ cell induction and significantly reduced ISG15+ cell upregulation (Fig. 4f-h).
186 Similarly, Janus kinase (JAK) inhibition downstream of IFNAR using JAK Inhibitor I[44]
187 blocked TNF-α-induced ISG15+ HPC upregulation (Extended Fig. 2g-h). Finally, TNF-α
188 upregulated the type I IFN-induced surface marker tetherin/BST-2 on HPCs (Extended
189 Fig. 2i and Supplementary Fig. 14), which was recently shown to be elevated on
190 dysfunctional NSCs in ageing neurogenic niches[28]. Collectively, these findings
191 demonstrated that TNF-α drives autocrine/paracrine type I IFN signalling in HPCs via
192 IFNAR and downstream JAKs likely mediated by IFN-β.

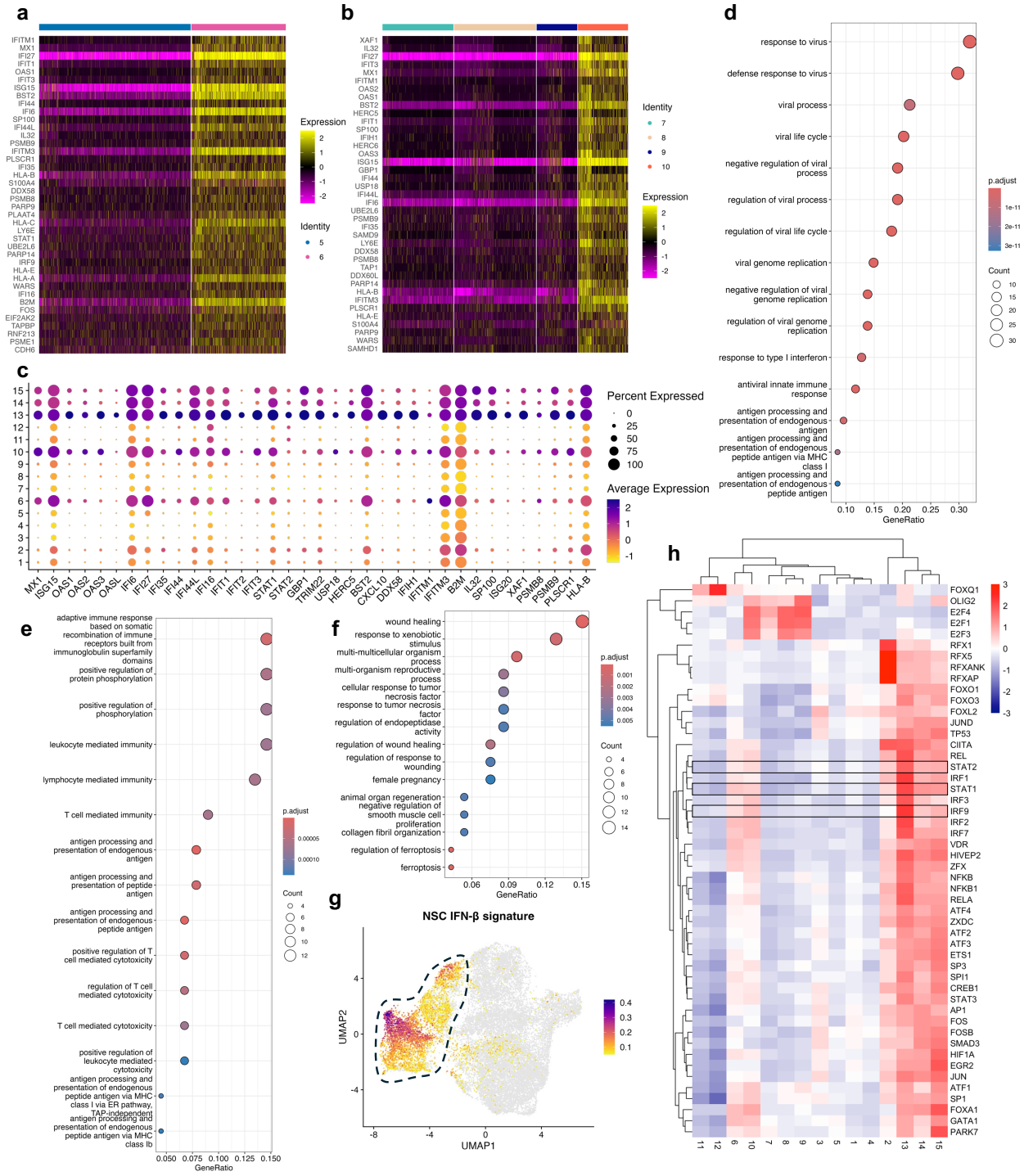

Fig. 3 | Chronic TNF-α drives the upregulation of type I IFN genes. a, Heatmap of top 40 upregulated genes based on log fold change in cluster six as compared to cluster five. **b**, Heatmap of top 40 upregulated genes based on log fold change in cluster ten as compared to cluster seven, eight, and nine. **c**, Dot plot showing the expression of interferon response genes across the cell clusters. **d**, Dot plot showing gene

198 ontology (GO) enrichment analysis of biological processes terms based on the top 100 genes positively
199 defining cluster 13. **e**, Dot plot showing gene ontology (GO) enrichment analysis of biological processes
200 terms based on the top 100 genes positively defining cluster 14. **f**, Dot plot showing gene ontology (GO)
201 enrichment analysis of biological processes terms based on the top 100 genes positively defining cluster
202 15. **g**, UMAP plot showing each cell scored against a NSC IFN-β transcriptional signature. The outlined
203 area highlight the of the signature with cluster 6, 10, 13, 14, and 15. **h**, Heatmap showing the mean activity
204 per cluster of the top 50 more variable transcription factors. STAT1, STAT2 and IRF9 is highlighted.
205

206 TNF-α-conditioned media from HPCs and differentiated progeny drive
207 CXCR3-dependent T cell chemotaxis

208 After elucidating the molecular mechanism of TNF-α-induced type I IFN signalling in
209 HPCs, we next investigated its functional consequences. Recent studies highlight T cell
210 infiltration into neurogenic niches in ageing and AD, with T cells found near NSCs[28,30,45–
211 49]. We found high levels of the type I IFN-regulated chemokines CXCL10 and CXCL11 in
212 the supernatant of HPCs and their differentiated progeny following TNF-α treatment. As
213 both chemokines promote T cell chemotaxis via the CXCR3 receptor [50], we hypothesised
214 that their secretion could mediate CXCR3-dependent T cell recruitment. We established
215 an *in vitro* transwell assay using primary human T cells from three healthy donors and
216 validated that recombinant CXCL10 promotes CXCR3-dependent chemotaxis of both
217 CD4+ and CD8+ T cells (Supplementary Fig.15-16).

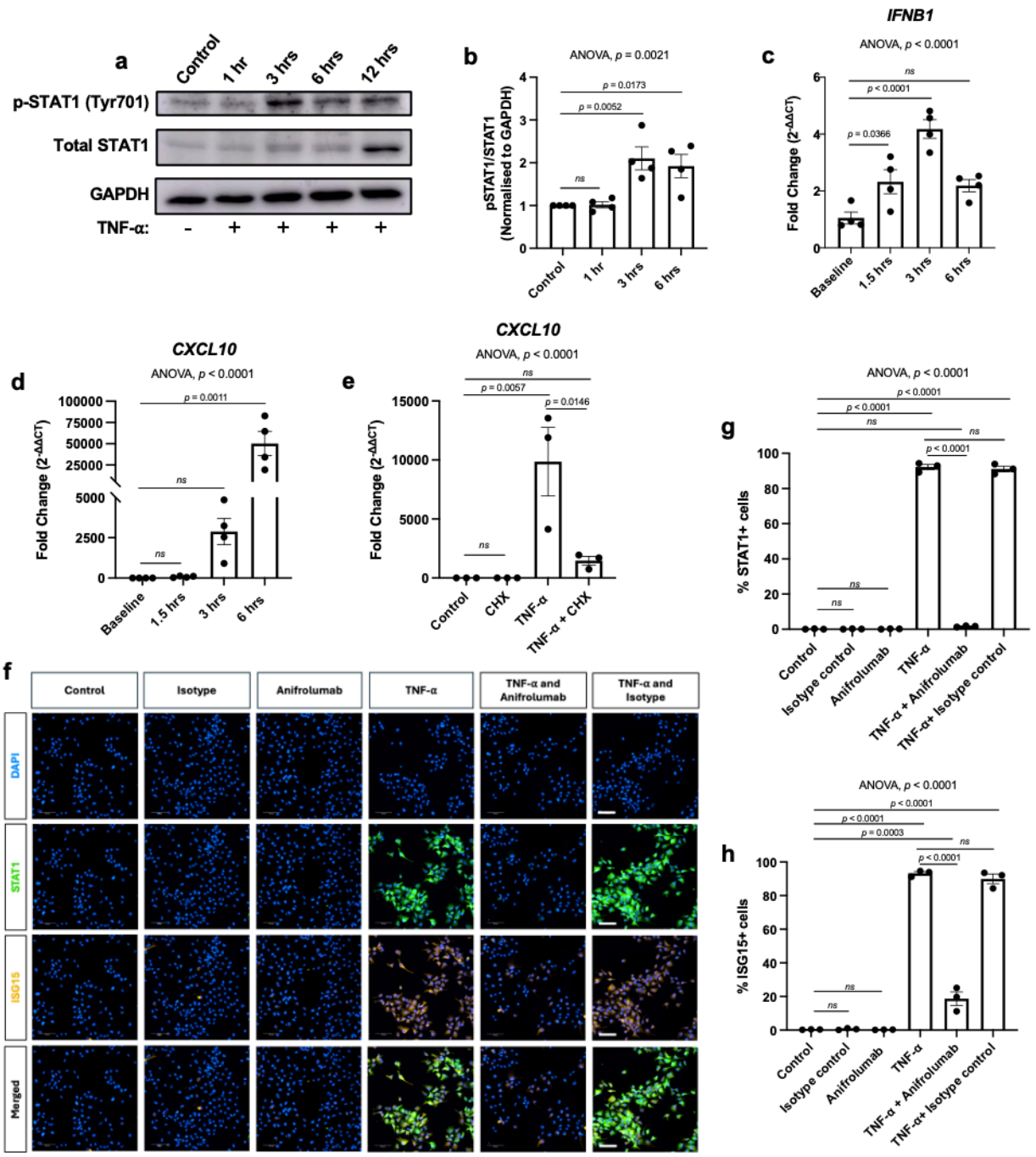

Fig. 4 | TNF-α drives type I IFN signalling in human hippocampal progenitor cells via autocrine/paracrine signalling via IFNAR. a, Representative western blots of four independent experiments showing the activation of STAT1 in HPCs treated with 1 ng/ml TNF-α for 1 hr, 3 hrs, 6 hrs, and 12 hrs. Cell lysates were probed for phosphorylated STAT1 (p-STAT1 Tyr701), total STAT1, and GAPDH as a loading control. **b**, Quantification of STAT1 activation in human hippocampal progenitor cells from **a**. pSTAT1 and STAT1 intensities were normalised to GAPDH intensity before calculating the fold change pSTAT1/STAT1 relative to control. Data represent mean ± SEM from four independent experiments.

226 Statistical analysis: one-way ANOVA followed by Bonferroni's multiple comparisons. **c**, RT-qPCR data
227 showing the relative gene expression of *IFNB1* in response to treatment with 1 ng/ml TNF-α. Data is
228 represented as mean ± SEM of four independent experiments. Statistical analysis: one-way ANOVA
229 followed by Bonferroni's multiple comparisons. **d**, RT-qPCR data showing the relative gene expression of
230 *CXCL10* in response to treatment with 1 ng/ml TNF-α. Data is represented as mean ± SEM of four
231 independent experiments. Statistical analysis: Kruskal-Wallis test followed by Dunn's post hoc correction.
232 **e**, RT-qPCR data showing the relative gene expression of *CXCL10* in HPCs treated for six hours with 10
233 μg/ml CHX or DMSO ± 1 ng/ml TNF-α. Data is represented as mean ± SEM of three independent
234 experiments. Statistical analysis: one-way ANOVA followed by Bonferroni's multiple comparisons. **f**,
235 Representative images of three independent experiments with similar results showing the expression of
236 STAT1 (green) and ISG15 (orange) on HPCs. Scale bar represents 100 μm. **g**, Quantification of the
237 percentage of STAT1+ cells based on **f**. Data represent mean ± SEM. Statistical analysis: one-way ANOVA
238 followed by Bonferroni's multiple comparisons. **h**, Quantification of the percentage of ISG15+ cells based
239 on **f**. Data represent mean ± SEM. Statistical analysis: one-way ANOVA followed by Bonferroni's multiple
240 comparisons.
241
242 We generated conditioned media (CM) from TNF-α–treated HPCs as well as from HPC-
243 derived cells differentiated under chronic TNF-α exposure, and assessed its ability to
244 induce CXCR3-dependent migration of activated primary human CD4+ and CD8+ T cells
245 (Fig. 5a–h). CM from both TNF-α–treated HPCs and their differentiated progeny
246 significantly enhanced the chemotactic index of CD4+ and CD8+ T cells. This effect was
247 significantly blunted by pre-treatment of the T cells with a CXCR3 antagonist, indicating
248 that the migratory response was primarily CXCR3-dependent. These findings suggest
249 that both HPCs and their differentiated progeny secrete chemokines capable of promoting
250 T cell migration through CXCR3 signaling.
251
252 As our data indicated TNF-α-induced *CXCL10* upregulation was mediated via the type I
253 IFN autocrine/paracrine signalling loop, we tested whether IFNAR or JAK inhibition
254 abrogated T cell chemotaxis in response to TNF-α-CM from HPCs (Fig. 6a-b).

255 Pharmacological blockage of both IFNAR and JAK independently abrogated the
256 chemotactic response of CD4+ T and CD8+ T cells towards chemokines secreted by
257 TNF-α-stimulated HPCs (Fig. 6c-d). These results indicated that the secretion of CXCR3
258 ligands by HPCs in response to TNF-α was dependent on the autocrine/paracrine type I
259 IFN signalling loop.

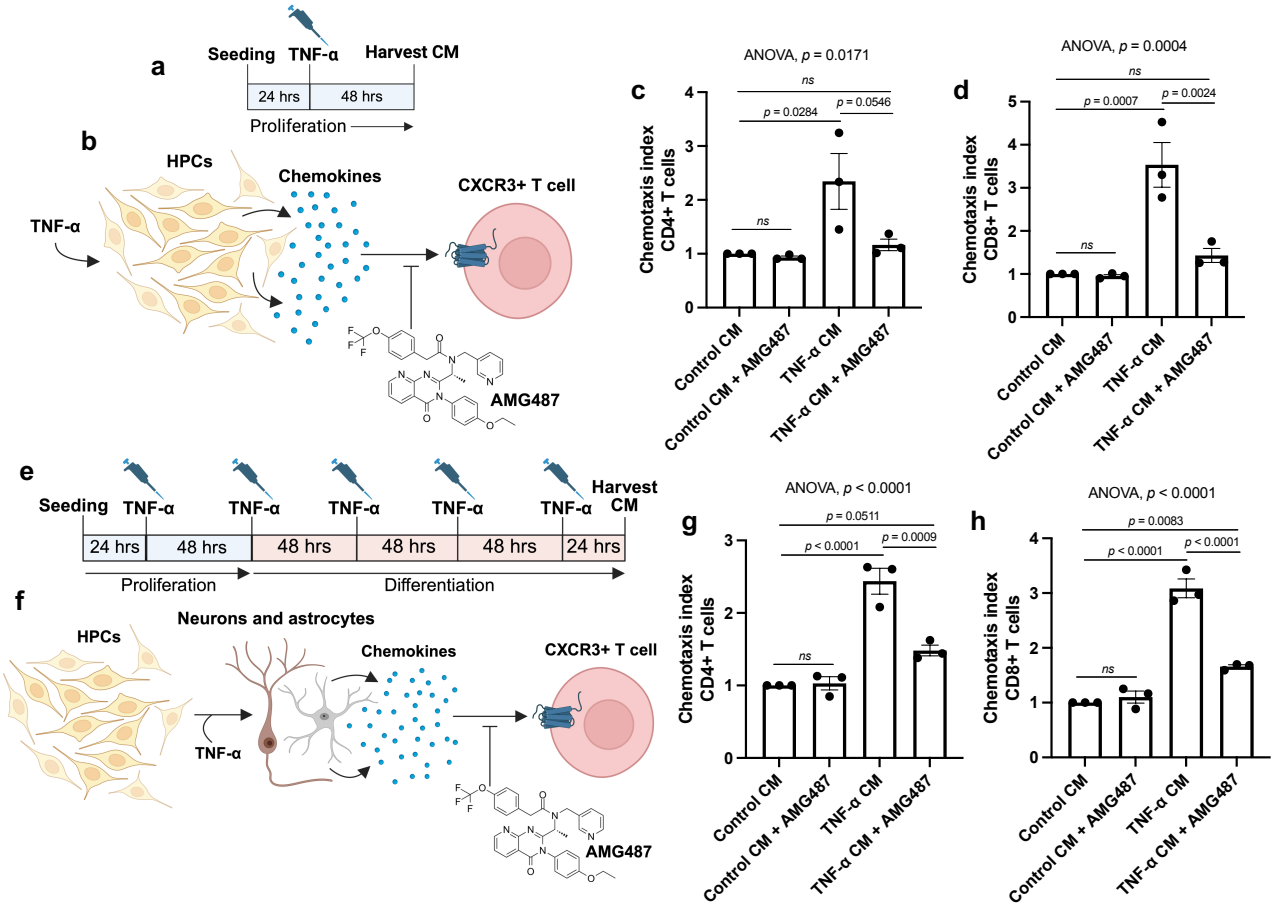

260

261 **Fig. 5 | TNF-α-conditioned media from proliferating and differentiating HPCs drive CXCR3-**
262 **dependent chemotaxis of primary, human T cells. a**, Schematic overview of the experimental design for
263 generating conditioned media (CM) from HPCs treated for ± 1 ng/ml TNF-α for 48 hrs. **b**, Chemokine
264 secretion by HPCs in response to TNF-α stimulation assessed for its ability to induce CXCR3-dependent T
265 cell chemotaxis. **c**, and **d**, Quantification of the chemotactic response (chemotaxis index) of **c** CD4+ T cells
266 and **d** CD8+ T cells treated ± 1 μM AMG487 or DMSO in response to control CM or TNF-α-CM from HPCs.
267 Data is represented as mean ± SEM of three healthy donors. Statistical analysis: one-way ANOVA followed
268 by Bonferroni's multiple comparisons test. **e**, Schematic overview of the experimental design for generating

269 CM from differentiated HPCs treated chronically ± 1 ng/ml TNF-α. **f**, Chemokine secretion by differentiated
270 HPCs in response to chronic TNF-α stimulation assessed for its ability to induce CXCR3-dependent T cell
271 chemotaxis. **g**, and **h**, Quantification of the chemotactic response (chemotaxis index) of **g** CD4+ T cells and
272 **h** CD8+ T cells treated ± 1 μM AMG487 or DMSO in response to control CM or TNF-α-CM from
273 differentiated HPCs. Data is represented as mean ± SEM of three healthy donors. Statistical analysis: one-
274 way ANOVA followed by Bonferroni's multiple comparisons test.
275

276 In addition to chemokine secretion, TNF-α upregulated the expression of adhesion
277 molecules in HPCs implicated in T cell interactions including *ICAM1* and *VCAM1*
278 (Supplementary Fig. 17). Notably, *ICAM1* expression was significantly increased after 3-
279 6 hours of TNF-α exposure and remained elevated on the HPC surface at 24 hours post-
280 treatment (Supplementary Fig. 18b).
281

282 Together, these findings demonstrated that TNF-α stimulation of HPCs promoted
283 CXCR3-dependent chemotaxis of primary human T cells *in vitro* through a type I IFN-
284 mediated autocrine/paracrine loop. Furthermore, TNF-α enhanced HPC expression of
285 adhesion molecules, potentially facilitating direct HPC–T cell interactions.
286
287
288
289
290

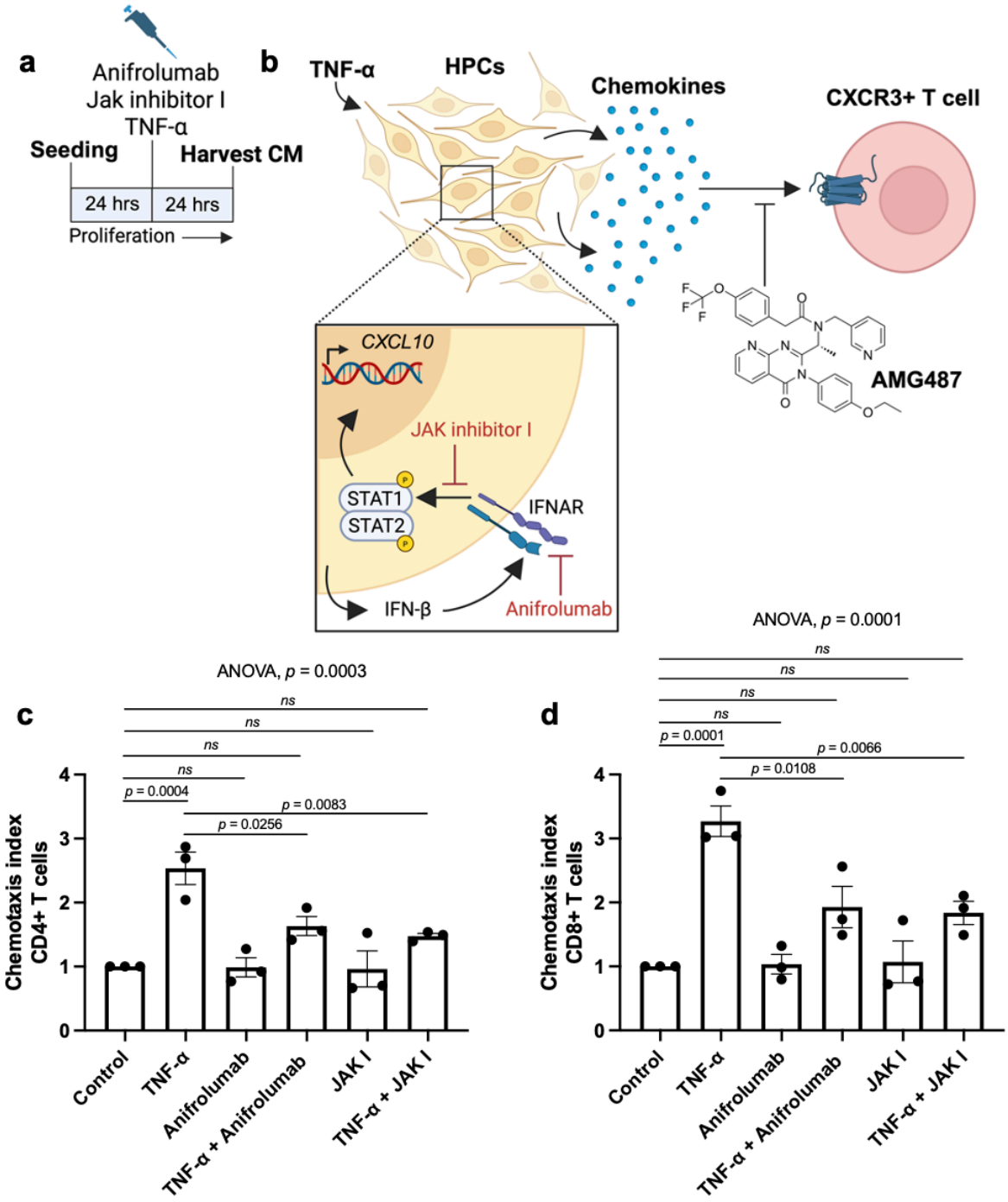

Fig. 6 | JAK and IFNAR signalling are indispensable for TNF-α-induced HPC chemokine secretion directing T cell chemotaxis. a, Schematic overview of the experimental design for generating conditioned media (CM) from HPCs treated ± 1 ng/ml TNF-α, ± 10 µg/ml anifrolumab (IFNAR antagonist), and ± 0.16 nM JAK inhibitor I for 24 hrs. **b**, The effect of IFNAR and JAK inhibition was evaluated for its ability to abrogate CXCR3-dependent T cell chemotaxis towards HPC TNF-α-CM. **c**, and **d**, Quantification of the chemotactic response (chemotaxis index) of **c** CD4+ T cells and **d** CD8+ T cells in response to the CM

generated as outlined in **a**. Data is represented as mean ± SEM of three healthy donors. Statistical analysis: one-way ANOVA followed by Bonferroni's multiple comparisons test.

Blocking IFNAR signalling rescues DCX$^+$ neuroblast loss induced by chronic TNF-α

Given the prominent activation of STAT1/STAT2 downstream of TNF-α, and the established role of STAT1 as a negative regulator of hippocampal neurogenesis and cognition[39,51–53], we hypothesised that chronic TNF-α may exert its antineurogenic effects via IFNAR-dependent type I interferon signalling. To test this, we administered the IFNAR-blocking antibody anifrolumab, which effectively suppressed TNF-α–induced ISG15 expression in differentiating HPCs (Supplementary Fig. 19), confirming inhibition of type I IFN signalling. As previously observed, chronic exposure to 1 ng/ml TNF-α selectively impaired the generation of DCX$^+$ neuroblasts without affecting the proportion of MAP2$^+$ neurons (Fig. 7a–c). Notably, IFNAR blockade fully rescued the loss of DCX$^+$ neuroblasts, implicating autocrine/paracrine type I IFN signalling as a key mediator of TNF-α–driven neurogenic deficits. These findings are consistent with prior evidence that disrupting type I IFN pathways can restore hippocampal neurogenesis in ageing models[54].

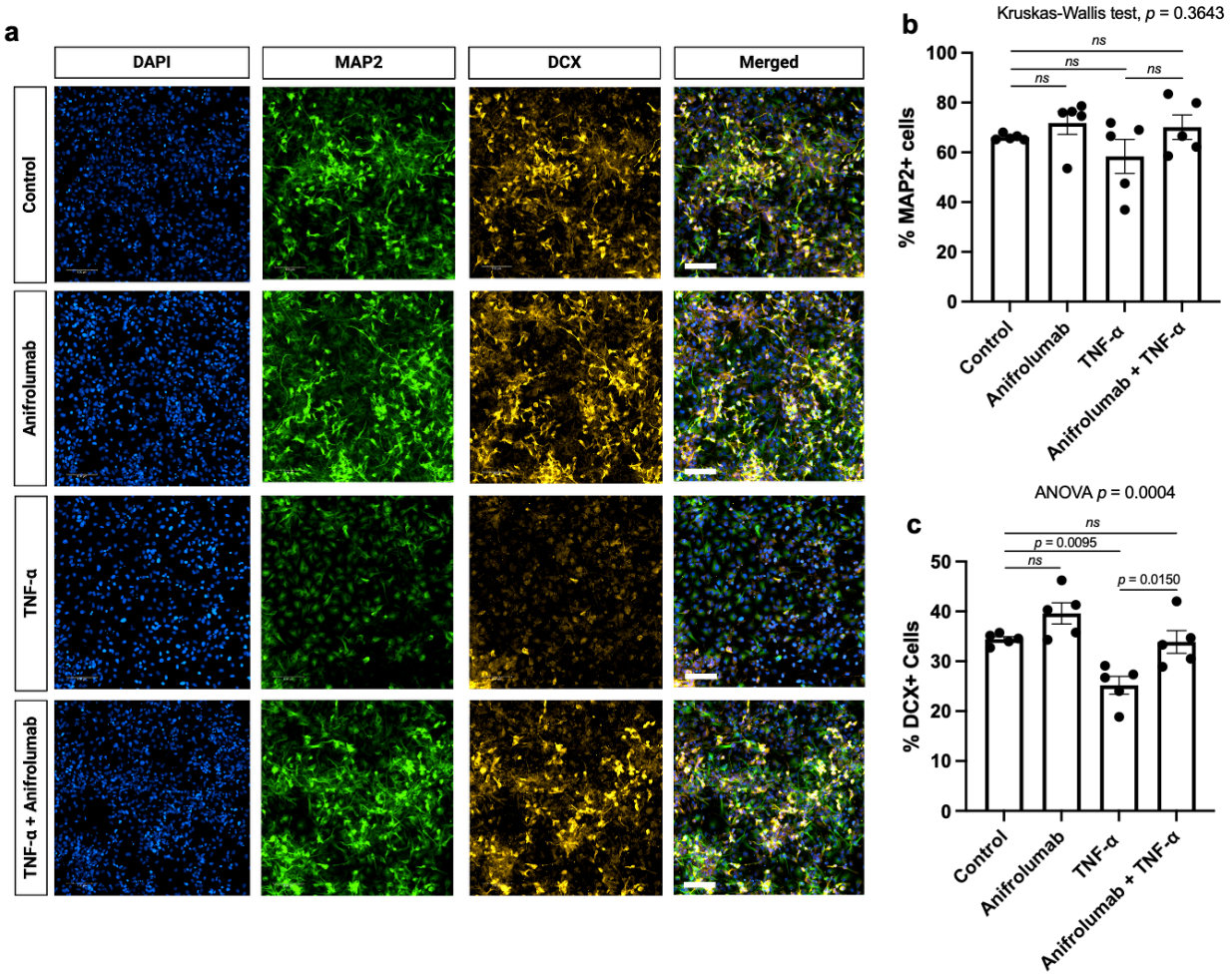

Fig. 7 | IFNAR blockage rescues the chronic TNF-α-induced decrease in the percentage of DCX+ neuroblasts. a, Representative images showing the expression of MAP2 (green) and DCX (orange) ion seven days differentiated HPCs treated chronically ± 1 TNF-α ± 10 µg/ml anifrolumab. Scale bar represents 100 µm. **b**, and **c,** Quantification of the percentage of **b** MAP2+ cells and **c** DCX+ cells respectively based on **a**. Data represent mean ± SEM from five independent experiments. Statistical analysis: **b** Kruskal-Wallis test followed by Dunn's post hoc correction and **c** one-way ANOVA followed by Bonferroni's multiple comparisons test.

Discussion

Emerging evidence implicates neuroinflammation, impaired AHN, and T cell accumulation within the hippocampal neurogenic niche as key features of ageing and neurodegenerative diseases[28–30]. However, the mechanistic links connecting these

329 phenomena remain unclear. Here, we hypothesised that chronic TNF-α exposure
330 functionally reprogrammes HPCs, diverting them from a neurogenic fate toward an
331 immune-defensive phenotype, parallelling recent observations in olfactory NSCs[27]. This
332 phenotypic switch may both impair AHN directly and promote T accumulation, which
333 could further suppress neurogenesis. Together, these effects may contribute to cognitive
334 deficits observed in ageing and neurodegeneration. Utilising a human *in vitro* model we
335 demonstrated that chronic TNF-α suppress hippocampal neurogenesis while promoting
336 CXCL10 secretion. To investigate the molecular mechanisms underlying these
337 observations, we performed scRNA sequencing, which unexpectedly revealed a type I
338 IFN transcriptional signature in HPCs and their differentiating progeny. Mechanistically,
339 we found that TNF-α engages a type I IFN signalling cascade in HPCs, driven by an
340 autocrine/paracrine IFN-β. Moreover, this pathway suppressed neurogenesis and
341 induced CXCR3 ligand secretion, promoting chemotaxis of activated primary human T
342 cells. Our data uncovered a previously uncharacterised TNF-α-IFN-β-IFNAR-CXCL10
343 axis that may exist in other CNS-resident cells and its role in reprogramming HPCs from
344 a neurogenic to an immune-defensive state under chronic inflammatory conditions.
345 Importantly, IFNAR antagonism restored TNF-α-induced neuroblasts loss and blocked T
346 cell recruitment, identifying IFNAR signalling as a dual-action candidate therapeutic target
347 for mitigating inflammation-induced neurogenic dysfunction.
348
349 The antineurogenic effect of TNF-α we observed closely mirrors findings from primary
350 NSCs and *in vivo* models[26,55–57], reinforcing the validity of our human cellular system.
351 Similarly, the TNF-α-induced impairment of neuronal morphological maturation[57,58] and

352 CXCL10 secretion align with previous reports in primary cells[59]. These parallels
353 underscore the physiological relevance of our model and support its utility for mechanistic
354 dissection of inflammation-driven neurogenic dysfunction. Future *in vivo* studies will be
355 critical to extend these findings.
356
357 While type I IFN signalling is well characterised in infectious diseases[60], its role in sterile
358 inflammation remains less understood, but increasingly recognised[61,62]. Our findings
359 identify a TNF-α-IFN-β-IFNAR axis in human HPCs, representing a novel mechanism of
360 type I IFN activation by an endogenous inflammatory cytokine in a CNS-resident
361 progenitor cell. Similar TNF-α-induced IFN-β responses have been reported in non-CNS
362 cell types, requiring IRF1 and NF-κB [40–42,63]. Consistent with this, we showed that TNF-α
363 induces *IFNB1* expression in HPCs via an NF-κB–dependent, protein synthesis–
364 independent mechanism that may involve IRF1. Whether the TNF-α-IFN-β-IFNAR axis
365 operates in CNS cell types beyond HPCs—such as microglia, where IFN signatures have
366 recently been identified across a broad range of sterile brain pathologies[64] remains an
367 important question for future investigations. Given IFNAR's ubiquitous expression[65],
368 HPC-derived IFN-β may act on surrounding niche cells, potentially amplifying local
369 inflammatory crosstalk.
370
371 Although type I IFNs are traditionally considered as antiviral and neuroprotective,
372 sustained or dysregulated signalling has been increasingly implicated in ageing[54,66] and
373 AD[67–69]. Elevated type I IFNs impair AHN[39,54] and promote cognitive deficits[54,68,70] both of
374 which can be reversed through IFNAR antagonism[54,68]. These cognitive impairments are

375 likely mediated, at least in part, by IFN-induced AHN dysfunction. Furthermore, type I
376 IFNs can directly promote amyloidogenic, neurotoxic processes[71]. Our data support the
377 pathogenic role for type I IFN signalling: notably, we found that TNF-α suppresses
378 neurogenesis via type I IFN signalling and shifts differentiating progenitors towards an
379 IFN-response, astroglial-like state. This is consistent with recent evidence that Zika virus,
380 which drives type I IFN signalling, promotes a molecular switch from neurogenesis
381 towards astrogliogenesis[72]**.** Thus, type I IFNs may represent a converging downstream
382 mechanism through which chronic inflammation impairs AHN and contributes to cognitive
383 decline in ageing and neurodegeneration.
384
385 T cells infiltrate neurogenic niches in the context of ageing and AD[28–30,45–49,73], and have
386 been demonstrated to modulate brain ageing and neuroregeneration[74,75]. Understanding
387 the mechanisms underlying their infiltration and interactions with brain resident cells is
388 therefore critical. We found that TNF-α treatment induces HPC chemokine secretion
389 promoting CXCR3-dependent chemotaxis of activated primary human T cells, suggesting
390 hippocampal NSCs may directly recruit T cells during neuroinflammation, consistent with
391 findings in murine olfactory NSCs[27]. This indicates a conserved mechanism across
392 neurogenic niches and species, where chronic TNF-α reprograms NSCs towards immune
393 cell recruitment. In addition to NSCs, microglial activation is reported to drive CXCL10-
394 mediated CD8+ T cell recruitment and promote aging-related white matter degeneration[76].
395 Thus, multiple CNS cell types likely cooperate in recruiting T cells via CXCR3 ligands in
396 ageing and neurodegeneration.
397

398 We demonstrated that IFNAR and JAK antagonism abolished T cell chemotaxis towards
399 TNF-α-stimulated HPC-derived CM, demonstrating that autocrine/paracrine type I IFN
400 signalling is the primary driver of CXCR3 ligand secretion. This mechanism parallels
401 findings in a nephritis model, where TNFR2-induced IFN-β autocrine signalling promotes
402 renal monocyte recruitment[41]. Of note, in the brain, type I IFN signalling in astrocytes
403 promotes brain metastasis by enhancing monocytic myeloid cell recruitment[77]. Beyond
404 promoting T cell chemotaxis, HPC-secreted CXCR3 ligands may exert direct deleterious
405 effects on within the neurogenic niche, as CXCR3 activation has been demonstrated to
406 drive hippocampal neural hyperexcitability[69,78,79].
407
408 As CXCL10 and CXCL11 are upregulated by IFN-γ[50], IFN-γ-producing CD8+ T cells
409 infiltrating ageing neurogenic niches[28] may promote further CXCR3 ligand secretion from
410 NSCs, potentially creating a feed-forward loop enhancing T cell recruitment. This may
411 explain why CD8+ T cells have been found in close proximity to NSCs[28]. Increasing the
412 number of CD8+ T cells in the hippocampus has been shown to decrease the number of
413 proliferative progenitors and DCX+ newborn neurons[29]. This effect is likely mediated by
414 IFN-γ secretion which has been shown to negatively affect NSCs[28]. Consistently, CXCL10
415 inhibition enhances neuroblast production[80], possibly by reducing T cell infiltration. Thus,
416 TNF-α may impair AHN both by driving antineurogenic type I IFN signalling in NSCs and
417 recruiting CD8+ T cells that suppress neurogenesis via IFN-γ. Blocking adaptive immune
418 cell infiltration into neurogenic niches may represent a therapeutic strategy for cognitive
419 decline in ageing and neurodegeneration. Given the low abundance of NSCs, future *in*

420 *vivo* studies are needed to determine their contribution to T cell recruitment in
421 neuroinflammation.

422 The TNF-α-induced functional switch we observed in human HPCs —from a neurogenic
423 to an immune responsive phenotype —may represent a protective adaptation to infection
424 or injury. Since neurogenesis is energetically costly, redirecting cellular resources to
425 mount an immune response could be advantageous for resolving the underlying pro-
426 inflammatory challenge.

427 Collectively, our results provide novel insights into how chronic TNF-α changes the fate
428 of human HPCs from neurogenesis towards immune functions, elucidating the molecular
429 mechanism underlying this switch. Furthermore, this work offers a novel explanation for
430 the emerging appearance of type I IFN signalling in ageing and neurodegeneration where
431 TNF-α levels are elevated and highlights HPCs as potential direct participants in the
432 progression of chronic inflammation.

433 Methods

434 Cellular model of hippocampal neurogenesis

435 We used the human hippocampal progenitor cell line (HPC0A07/03A; ReNeuron LTD.,
436 Surrey, United Kingdom), derived from a first-trimester female foetus ethically approved
437 under UK and US guidelines, as a cellular model for hippocampal neurogenesis as
438 previously described[33,34,36,81]. The cell line was immortalised using the c-*mycER*^{TAM} gene
439 to conditionally proliferate in presence of 100 nM 4-hydroxy-tamoxifen (4-OHT) (Sigma
440 Aldrich, Cat No. H7904), 10 ng/mL human basic fibroblast growth factor (bFGF)

441 (Peprotech, Cat No. 100-18B-500) and 20 ng/mL human epidermal growth factor (EGF)
442 (Peprotech, Cat No. AF100-15–500) and spontaneously differentiate in their absence.
443 The cells were cultured as previously described[82] on laminin (Gibco, Cat No. 23017015)
444 coated culture vessels (Nunclon, Denmark) at 37 °C, 5 % CO2.

445 TNF-α-treatments

446 The HPCs were treated with TNF-α (Peprotech, Cat No. 300-01A) for the duration and
447 with the concentrations indicated in the individual experiments.

448 Immunocytochemistry

449 Cells were washed with PBS and fixed in 4% paraformaldehyde (in PBS) for 15 min at
450 room temperature. Cells were permeabilised and blocked for 1 h at room temperature in
451 blocking buffer: 0.3% Triton X-100 (Sigma, Cat No. X100) and 5% normal donkey serum
452 (Bio-Rad, Cat No. C06SB) in PBS. For TNFR1 and TNFR2 staining, a non-permeabilising
453 block (5% normal donkey serum in PBS) was used. Primary antibodies (Supplementary
454 Table 1), diluted in blocking buffer, were applied overnight at 4 °C. The following day, cells
455 were washed 3× with PBS and incubated with secondary antibodies (Supplementary
456 Table 1) in blocking buffer for 2 h at room temperature, protected from light. 300 nM DAPI
457 (Sigma, Cat No. 62248) in PBS was applied for 5 min at room temperature. Cells were
458 then washed 4× with PBS and stored at 4 °C in PBS containing 0.05% sodium azide
459 (Merck, Cat No. S2002).

460 High-content imaging and analysis

461 Immunostained cells were imaged using the Opera Phenix Plus High-Content Screening
462 System (PerkinElmer). Imaging was performed in a single focal plane using a 20× water-

463 immersion objective. A minimum of 9 fields per well were acquired from 96-well plates
464 and averaged to generate a mean per well. Channels were captured using the following
465 excitation/emission settings: DAPI (ex 385 nm/em 425–475 nm), Alexa Fluor 488
466 (ex 488 nm/em 500–550 nm), and Alexa Fluor 555 (ex 561 nm/em 609–644 nm). A
467 minimum of three technical replicates per condition were imaged and averaged for each
468 biological replicate. Images were analysed using Harmony software (PerkinElmer).
469 Briefly, cells were segmented using the *Find Nuclei* building block. Morphological
470 parameters were calculated using *Calculate Morphological Properties*, and nuclei smaller
471 than 50 µm² or larger than 500 µm² were excluded to remove apoptotic bodies and
472 artefacts. Cells at image borders were also excluded. Cytoplasmic or nuclear signal
473 intensity was quantified using *Find Cytoplasm*, *Find Morphological Properties*,
474 and *Calculate Intensity Properties* building blocks. Positive cells were identified using
475 the *Select Population* building block by applying a per-plate intensity threshold based on
476 control wells. The percentage of positive cells was calculated using the *Define Results*
477 building block.

478 RNA extraction, cDNA synthesis, and RT-qPCR

479 HPCs (3.5×10^5 cells per well) were seeded in 6-well plates coated with 20 µg/mL mouse
480 laminin (Sigma, Cat No. L2020,). Cells were treated the following day as indicated. For
481 lysis, media were removed, wells were washed with PBS, and cells were lysed in 350 µL
482 Buffer RLT Plus (Qiagen, Cat No. 74134) supplemented with 1:100 2-mercaptoethanol
483 (Bio-Rad, Cat No. 1610710). Lysates were scraped, transferred to microcentrifuge tubes,
484 vortexed, and stored at –80 °C. Total RNA was extracted using the RNeasy Plus Mini Kit
485 (Qiagen, Cat No. 74134,) following the manufacturer's instructions, and RNA

concentrations were measured using a NanoDrop spectrophotometer (Thermo Fisher Scientific). Extracted RNA (200 ng) was reverse transcribed using the High-Capacity cDNA Reverse Transcription Kit (Applied Biosystems, Cat No. 4368813) following the manufacturer's protocol. The thermal cycler program (Biometra Trio series, Analytik Jena) used for cDNA synthesis is provided in Supplementary Table 2. qPCR reactions contained 5 µL cDNA (1:4 dilution in nuclease-free water), 10 µL SYBR Green Master Mix (PCR Biosystems, Cat No. PB20.11-05,), 4 µL nuclease-free water, and 1 µL primer mix (10 pmol), in a total volume of 20 µL. Reactions were run in triplicate in 384-well plates (Applied Biosystems, Cat No. 4309849,) on a QuantStudio 5 Real-Time PCR System (Applied Biosystems) using the cycling protocol described in Supplementary Table 3. Data were analysed with QuantStudio Design & Analysis Software (v1.5.1), and relative gene expression was calculated using the 2^–ΔΔCt method with GAPDH as the reference gene. Primer sequences are provided in Supplementary Table 4.

499 ## Western blotting

500 HPCs (3–6 × 10^5 cells per well) were seeded in laminin-coated 6-well plates (Thermo
501 Fisher Scientific, Cat No. 140675). Cells were treated the following day as indicated. Cells
502 were washed with PBS and lysed in 150 µL 1 × Laemmli buffer (Bio-Rad, Cat. No.
503 1610747) diluted in PBS and supplemented with 355 mM β-mercaptoethanol (Bio-Rad,
504 Cat. No. 1610710). Lysates were scraped, boiled for 5 min at 95 °C, and stored at –80 °C
505 until analysis. Proteins were resolved by 10% SDS–PAGE and transferred to PVDF
506 membranes (Thermo Fisher Scientific, Cat. No. 88518). Membranes were blocked for 1 h
507 at room temperature in PBS containing 5% milk and 0.1% Tween-20, then washed 3×
508 (10 min each) with PBS + 0.5% Tween-20. Primary antibodies (Supplementary Table 5)
509 were applied overnight at 4 °C in blocking buffer. After washing, membranes were
510 incubated with HRP-conjugated secondary antibodies for 1 h at room temperature,
511 followed by 3× washes in PBS + 0.5% Tween-20. Detection was performed using Clarity
512 Max ECL (Bio-Rad, Cat. No. 1705062,) for STAT proteins and Clarity ECL (Bio-Rad, Cat.
513 No. 1705061) for GAPDH, each for 4 min. Membranes were imaged on an ImageQuant
514 800 Imager (Amersham), and band intensities were quantified using Image Studio.

515 ## Western blotting quantifications

516 Band intensities for phosphorylated and total STAT proteins, as well as GAPDH, were
517 measured using Image Studio. Phosphorylated and total STAT signals were normalised
518 to the corresponding GAPDH signal. The ratio of phosphorylated to total STAT protein
519 was then calculated for each sample and expressed relative to control.

Statistical analysis

Analyses were performed using GraphPad Prism (v10.4.1) and R (v4.3.2) with rstatix (v0.7.2). Normality was assessed by Q–Q plots and Shapiro–Wilk test, and variance homogeneity by Levene's test. Results are reported as mean ± SEM, with statistical significance set at $p < 0.05$. The specific test and sample size are stated in each figure legend. For normally distributed data, unpaired Student's t-test was used for two-group comparisons, and one-way ANOVA with Bonferroni post hoc for >2 groups. If variances were unequal, we applied Welch's t-test or Welch's ANOVA with Games–Howell correction. Non-normally distributed data were analysed using the Wilcoxon rank-sum test for two groups or Kruskal–Wallis test with Dunn's post hoc for multiple groups.

NF-kB nuclear translocation assay

HPCs (1.2×10^4 cells per well) were seeded in laminin-coated 96-well plates. The following day cells were treated ± 10 ng/mL TNF-α and fixed after 0, 15, 30, 45, and 60 min, and 2, 3, 4, 24, and 48 h. Cells were immunostained for NF-κB p65 and counterstained with DAPI. High-content imaging was performed on an Opera Phenix (PerkinElmer), and images were analysed using Harmony software (PerkinElmer). Nuclear and cytoplasmic NF-κB p65 signal intensities were measured, and the nuclear fraction of p65 fluorescence was calculated as described below:

$$Fraction\ of\ nuclear\ fluorescence = \frac{Nuclear\ intensity}{Nuclear\ intensity + cytosol\ intensity}$$

539 ## Cytokine and chemokine secretion analysis

540 HPCs (1.2×10^5 cells) were seeded in laminin-coated 24-well plates (Thermo Fisher
541 Scientific, Cat. No. 142475). The following day, the media was replaced with proliferation
542 medium ± TNF-α. After 24 h and 48 h, supernatants were collected and stored at –80 °C.
543 For differentiation, the cells cultured in proliferation media for 48 hours were washed twice
544 with differentiation medium for 30 min, then cultured in differentiation medium ± TNF-α.
545 Supernatants were collected after 24 h, 48 h, and 7 d. IL-6 levels were quantified using a
546 human IL-6 ELISA Kit (BioLegend, Cat. No. 430504). A 13-plex panel of human pro-
547 inflammatory chemokines (Supplementary Table 6) was analysed using a multiplex bead-
548 based assay kit (BioLegend, Cat. No. 740985). Data was acquired using a FACSCanto II
549 (BD Biosciences) flow cytometer and analysed using the LEGENDplex data analysis
550 software suite (BioLegend).

551 ## Differentiation assay for immunocytochemistry

552 HPCs were seeded at 1.2×10^4 cells per well in laminin-coated 96-well plates (Thermo
553 Fisher Scientific, Cat. No. 140675) in proliferation medium containing 4-OHT, bFGF, and
554 EGF. The following day, the medium was replaced with proliferation medium ± TNF-α.
555 After 48 h, cells were washed twice with differentiation medium (no 4-OHT, bFGF, or
556 EGF) for 30 min, then cultured in differentiation medium ± TNF-α for 7 d, with media
557 changes every 48 h. In a subsequent experiment, cells were treated with ± 1 ng/mL TNF-
558 α and ± 10 μg/mL anifrolumab.

559 ## Neurite outgrowth analysis

560 Neurite outgrowth of DCX+ and MAP2+ cell populations was assessed using Harmony
561 (PerkinElmer). Cells were identified as described in the High-Content Imaging and
562 Analysis section. Neurites were detected using the 'Find Neurites' building block, and
563 neurite morphology parameters, including the length of the longest neurite, were
564 quantified.

565 ## Cell culture and treatment for the single-cell RNA sequencing

566 ### *Proliferation*

567 HPCs were seeded into 20 µg/ml mouse laminin (Sigma, Cat. No. L2020) coated T175
568 flasks (Sigma, Cat. No. L2020) at 2.9×10^6 cells for control or low TNF-α (0.1 ng/mL)
569 conditions, and 5×10^6 cells for high TNF-α (1 ng/mL) conditions. The following day, the
570 media was replaced with proliferation medium ± TNF-α. The cells were harvested after
571 48 h.

572 ### *Differentiation*

573 HPCs were cultured as described above in proliferation medium ± TNF-α for 48 hrs. Next,
574 the media was changed to differentiation media ± 0.1 ng/ml TNF-α or 1 ng/ml TNF-α. The
575 HPCs were allowed to differentiate for seven or fourteen days. To mimic a chronic TNF-
576 α-mediated proinflammatory environment the differentiation media was changed every 48
577 hours to fresh differentiation media ± 0.1 ng/ml TNF-α or 1 ng/ml TNF-α. After seven or
578 fourteen days of differentiation the cells were harvested.

579 ## Harvesting cells for single-cell RNA sequencing

580 On the day of harvest, medium was removed and cells washed with pre-warmed DPBS
581 (Gibco, Cat. No. 14190144). Cells were detached using pre-warmed Accutase (Gibco,
582 Cat. No. A1110501) at 37 °C, 5% CO_2 for 5–10 min, harvested with pre-warmed
583 DMEM/F12 (Gibco, Cat. No. 21331020), and centrifuged at 100 × g for 5 min. Pellets were
584 gently resuspended in 1 mL of the warm proliferation or differentiation medium. Viability
585 was confirmed at ≥ 85% using Trypan Blue (Thermo Fisher Scientific, Cat. No.
586 15250061,) and a hemocytometer before proceeding to antibody labelling.

587 ## Cell surface staining with hashtag oligonucleotide antibodies

588 For 3′ scRNA-seq multiplexing on the 10x Genomics Chromium system, samples were
589 labelled with TotalSeq™-B anti-human hashtag oligonucleotide (HTO) antibodies
590 targeting CD298 and β2-microglobulin (BioLegend: Hashtag 1 Cat. No. 394631; Hashtag
591 2 Cat. No. 394633; Hashtag 3 Cat. No. 394635). Optimal antibody concentration (1:5,000;
592 125 ng/mL) was determined by titrating PE-conjugated anti-CD298 (BioLegend, Cat. No.
593 341704) and anti-B2M (BioLegend, Cat. No. 316305) at a 1:1 equimolar ratio, followed
594 by ICC to confirm 100% labelling with minimal background. Samples were individually
595 labelled with HTOs prior to pooling at the sequencing facility.

596

597 1×10^6 cells per sample were pelleted (300 × g, 5 min, 4 °C) and resuspended in 45 µL
598 Cell Staining Buffer (CSB) (BioLegend, Cat. No. 420201). Cells were blocked with 5 µL
599 TruStain FcX™ (BioLegend, Cat. No. 422301) for 10 min at 4 °C. TotalSeq™-B HTO
600 antibodies were diluted 1:2,500 in CSB and mixed 1:1 with blocked cells to reach a final
601 concentration of 1:5,000. Samples were incubated for 30 min at 4 °C. Cells were washed

602 3× in CSB (300 × g, 5 min, 4 °C) resuspending using wide-bore pipette tips (Starlab, Cat.
603 No. E1011-9618). Final concentration was adjusted to 700–1,200 cells/μL, assuming
604 ~50% cell loss. Cell suspensions were filtered through 40 μm Flowmi™ Cell Strainers
605 (Bel-Art, Cat. No. H13680-0040), and viability (>80%) was confirmed before proceeding
606 to the 10x Genomics workflow. All steps were performed on ice.

607 Single-cell capture, cDNA library preparation, and sequencing

608
609 HTO-labelled samples were pooled and processed by the Genomics Research Platform
610 at Guy's & St Thomas's Hospital (London, UK). The differentiation samples (three pools)
611 and the proliferation samples (one pool) were delivered to the facility on separate days.
612 Equal cell numbers were combined, and 18,000 cells per pool were loaded onto separate
613 lanes of the 10x Chromium X instrument (10x Genomics) for droplet-based single-cell
614 capture. cDNA libraries were prepared using the Chromium Single Cell 3′ Reagent Kit v3
615 (10x Genomics, Cat. No. PN-1000268,). Libraries were sequenced on an Illumina
616 NextSeq 2000 system using 50 bp paired-end reads.

617

618 Read alignment and sample demultiplexing

619 FASTQ files from gene expression and HTO libraries were processed using Cell Ranger
620 v7.1 (10x Genomics) with the cellranger multi pipeline. Data were imported into R (v4.3.2)
621 using Seurat v5 via the Read10X() function, returning UMI and HTO count matrices. Cells
622 with barcodes present in both matrices were retained, and RNA counts were used to
623 create a Seurat object (CreateSeuratObject()), with HTO data added as an independent
624 assay (CreateAssayObject()). HTO data were normalised using centred log-ratio
625 transformation and demultiplexed using HTODemux(assay = 'HTO') with default

626 parameters. Only singlets with confident HTO classification were retained for downstream
627 analysis.

628 Quality control

629
630 QC was performed separately on merged Seurat objects for differentiation and
631 proliferation samples. At the cell level, cells were excluded if they had >15% mitochondrial
632 gene expression, a novelty score ($\log_{10}$[genes/UMIs]) <0.8, <800 or >8,000 genes, or
633 <1,000 or >45,000 transcripts. This yielded 22,133 high-quality cells (15,053 derived from
634 differentiation samples; 7,080 derived from proliferation samples). At the gene level,
635 genes not expressed in any cells or expressed in ≤5 cells were excluded. Post-filtering,
636 26,288 genes were retained in the differentiation dataset and 21,951 in the proliferation
637 dataset.

638 Normalisation, dimensionality reduction, and clustering

639 The differentiation and proliferation Seurat objects were merged and normalised
640 using sctransform (v2) from Seurat. Dimensionality reduction was performed using
641 principal component analysis (PCA) on the top 3,000 highly variable genes. An ElbowPlot
642 indicated that the first 50 principal components captured the majority of variance in the
643 dataset which was used for downstream analysis. We constructed a shared nearest
644 neighbour graph using FindNeighbors(), tested clustering across resolutions from 0.1 to
645 1.2 (FindClusters()), and visualised cellular heterogeneity via UMAP (RunUMAP(dims =
646 1:50)), displayed with DimPlot(reduction = "umap").

647 Cluster annotation

648

649 Clusters were initially over-resolved using high-resolution settings and subsequently
650 merged if they lacked distinct marker genes, were not biologically meaningful, or shared
651 multiple canonical markers. This iterative approach—clustering, merging, and re-
652 clustering—was guided by marker gene expression. Cluster markers were identified using
653 the FindAllMarkers() function in Seurat, applying Wilcoxon rank-sum testing to compare
654 each cluster against all others. Marker genes were required to be expressed in ≥25% of
655 cells within the cluster and show positive differential expression ($\log_2$ fold change ≥0.25).
656 Ultimately, 15 clusters were identified and annotated based on culture condition,
657 treatment, cell cycle stage, and canonical marker expression.

658 Functional enrichment analysis

659 [111]Gene Ontology (GO) over-representation analysis was performed using the
660 ClusterProfiler package[83]. The top 100 differentially expressed genes (ranked by log fold
661 change) between clusters were used as input. Raw p-values < 0.05 were considered for
662 enrichment. Multiple testing correction was performed using the Benjamini–Hochberg
663 method, with the default adjusted p-value threshold of 0.2.

664 Transcription factor activity inference

665 Transcription factor (TF) activity was inferred using decoupleR (v2.8)[84]. CollecTRI[85] was
666 retrieved via OmnipathR[86]. The univariate linear model generates a TF enrichment score
667 by fitting a linear model of gene expression based on TF–gene interaction weights. The
668 t-value of the slope (ULM score) indicates TF activity: positive scores denote activation
669 and negative scores indicate inactivity.

670 ## Gene module scoring for NSC-specific type I IFN response signature

671 Cells were scored using a 300-gene NSC-specific type I IFN response signature derived
672 from murine SVZ NSCs treated *ex vivo* with IFN-β[38]. Average gene set expression per
673 cell was calculated using the Seurat function AddModuleScore().

674 ## Gene module scoring for human immature dentate granule cell signature

675 Cells were scored against the top 20 genes from a gene list identifying human immature
676 dentate granule cells[9]. Average gene set expression per cell was calculated using the
677 AddModuleScore() funtion.

678 ## Conditioned media experiment for immunocytochemistry

679 To generate conditioned media (CM) 3 x 10^5 HPCs were seeded into six well plates coated
680 with 20 µg/ml mouse laminin (Sigma, Cat. No. L2020). The following day, the media was
681 replaced with fresh media ± 0.1 ng/ml, 1 ng/ml, or 10 ng/ml TNF-α. After 24 hours, media
682 was switched to control media without TNF-α and cells were cultured for an additional 24
683 hours before CM collection. This approach captured HPC-secreted factors in response to
684 TNF-α while eliminating residual TNF-α. To assess CM effects on IFN-regulated protein
685 ISG15 expression, HPCs were seeded into laminin-coated 96-well plates. The next day,
686 media was replaced with 70% CM mixed with 30% fresh media to maintain cell viability.
687 After 48 hours, cells were fixed, immunostained, and imaged to quantify the percentage
688 of $ISG15^+$ HPCs.

689 ## Protein synthesis inhibition

690 To investigate the requirement of *de novo* protein synthesis in the TNF-α-induced
691 upregulation of candidate genes, we utilised the global protein translation inhibitor,
692 cycloheximide. The HPCs were treated as described in the results section with 10 µg/ml
693 cycloheximide (Merck, Cat. No. 01810).

694 ## Blocking NF-kB signalling

695 Cells were seeded in six-well plates coated with 20 µg/ml mouse laminin (Sigma, Cat.
696 No. L2020). After 24 hours, the media was replaced with media containing 10 µM JSH23
697 (Abcam, Cat. No. ab144824) dissolved in 100% dimethyl sulfoxide (DMSO) or with DMSO
698 as control. The final DMSO concentration in both groups was 0.1%. Following a 30-minute
699 pre-treatment, 1 ng/ml TNF-α was added as indicated in the results section, and cells
700 were harvested for gene expression analysis.

701 ## Probing the dependency of IFNAR in TNF-α-induced type I IFN signalling

702 To assess IFNAR dependency in TNF-α-induced type I IFN signalling, HPCs (1.2 × 10^4)
703 were seeded in laminin-coated 96-well plates. The following day, cells were treated with
704 or without 10 µg/ml anifrolumab (Bio X Cell, Cat. No. SIM0022), an anti-IFNAR1 antibody,
705 or isotype control (Bio X Cell, Cat. No. SIM0014), and with or without 1 ng/ml TNF-α. After
706 24 h, cells were fixed and stained for ISG15, STAT1, and DAPI. High-content imaging
707 quantified ISG15+ and STAT1+ cells as described.

708 ## Blocking JAK activity

709

710 1.2 × 10^4 HPCs were seeded in laminin-coated 96-well plates (Thermo Fisher Scientific,
711 Cat. No. 167008). The following day, cells were treated with or without 16 nM JAK inhibitor
712 I (Cayman Chemical, Cat. No. CAY15146) and with or without 1 ng/ml TNF-α. After 24 h,
713 media was removed, cells fixed and stained, and high-content imaging was used to
714 quantify ISG15+ HPCs.
715

716 Evaluating cell surface protein expression with flow cytometry

717 Cells were cultured in laminin-coated T75 flasks (Sigma, Cat. No. L2020) and treated ± 1
718 ng/ml TNF-α for 24 h. Cells were detached with Accutase (Sigma, Cat. No. A1110501)
719 for five min in the incubator, harvested, centrifuged, and resuspended in PBS. Cells were
720 stained with Zombie NIR viability dye (BioLegend, Cat. No. 423105; 1:2000 in PBS) for
721 15 min at room temperature. Cells were washed and stained with antibodies
722 (Supplementary Table 7) at 1:100 in staining buffer (PBS + 10 mM HEPES, 2 mM EDTA,
723 0.5% FCS) for 40 min at 4 °C. After washes, cells were resuspended in staining buffer.
724 Data were acquired on a BD FACS Canto II using FACSDiva v9.2 and analysed with
725 FlowJo v10.10.

726 Isolating peripheral blood mononuclear cells from leukocyte cones

727
728 Peripheral blood mononuclear cells (PBMCs) were isolated from leukocyte cones
729 obtained from three healthy donors via NHS Blood and Transplant (NHSBT, Tooting, UK).
730 Donors provided generic consent for research use. Leukocyte cones were cleaned with
731 ethanol and processed in a biosafety cabinet. Blood was drained into a 50 ml tube which
732 was topped up to 50 ml with PBS containing 2% FCS. After gently mixing it was
733 centrifuged at 800 × g for 10 minutes. The pellet was resuspended 1:1 in DPBS and

734 layered onto 15 ml Ficoll-Paque PLUS (Cytiva, Cat. No. 17144002). After centrifugation
735 at 450 × g for 30 minutes with minimal acceleration and no brake, the buffy coat was
736 collected, washed twice with cold DPBS, and centrifuged at 400 × g for 10 minutes at
737 4°C. A final centrifugation step at 200 × g for 10 minutes at 4°C was performed to reduce
738 platelet contamination. Cells were counted, resuspended in freezing media (90% FBS,
739 10% DMSO) at 360–600 × 10^6 cells/ml, aliquoted into cryovials, frozen overnight at −80°C
740 in a Mr. Frosty container, and transferred to liquid nitrogen for long-term storage. Each
741 vial contained 9–15 × 10^6 cells.

742 Chemotaxis assay

743 *T cell activation and expansion protocol*

744 PBMC cryovials were thawed and seeded in T75 flasks at 37°C with 5% CO_2 in complete
745 RPMI (10% FCS (Thermo Fisher Scientific, Cat. No. 26140079), 1% penicillin-
746 streptomycin (Thermo Fisher Scientific, Cat. No. 15140122)). After 24 hours, nonadherent
747 lymphocytes were collected, centrifuged, and cultured in complete RPMI supplemented
748 with 100 IU/ml recombinant human IL-2 (BioLegend, Cat. No. 689104) and 2.5 µg/ml
749 phytohemagglutinin-L (PHA-L) (Thermo Fisher Scientific, Cat. No. 00-4977-93) in fresh
750 T75 flasks. After 48 hours, cells were harvested, washed, and resuspended in complete
751 RPMI with 100 IU/ml IL-2. The cells were cultured for a total of 10 days and were
752 resuspended in fresh complete RPMI media supplemented with 100 IU/ml IL-2 every
753 other day.

754 *Transwell chemotaxis assay*

755 Transwell migration assays were performed using 96-well transwell plates with 5 µm pore
756 membranes (Corning, Cat. No. 3387). Upper wells were coated overnight with 2% BSA
757 in PBS to prevent cell adhesion and washed thrice with PBS the following day. Activated
758 lymphocytes were harvested, washed, and resuspended at 4–5 × 10^6 cells/ml in
759 migration media (complete RPMI diluted 1:10 in neat RPMI), HPC proliferation media, or
760 HPC differentiation media as appropriate. For CXCR3 dependency assays, cells were
761 pretreated with 1 µM AMG487 (Cayman Chemical, Cat. No. 28416) or DMSO control for
762 30 minutes at 37°C with rotation. 75 µl cell suspension were added to upper chambers.
763 Lower chambers were filled with 235 µl media containing 100 ng/ml recombinant human
764 CXCL10 (R&D Systems, Cat. No. 266-IP), TNF-α-conditioned media (CM) from
765 proliferating or differentiating HPCs, or CM from HPCs treated ± TNF-α, JAK inhibitor I,
766 or anifrolumab. After 3 hours at 37°C, migrated cells in the lower chamber were collected
767 into 96-well plates for analysis.

768 *Flow cytometry of migrated cells*

769 Migrated cells were collected by spinning the plate at 2000 rpm for 1 min and washed
770 with 200 µl DPBS. Cells were stained with Zombie NIR viability dye (BioLegend, Cat. No.
771 423105; 1:2000 in DPBS) for 15 min at room temperature in the dark, followed by
772 quenching with 100 µl DPBS and centrifugation. For CXCR3 surface expression, cells
773 were incubated with anti-CXCR3 antibody (1:100 in staining buffer: DPBS + 10 mM
774 HEPES + 2 mM EDTA + 0.5% FCS) at 37°C for 15 min. Next cells were stained with a
775 master mix of antibodies (Supplementary Table 8; 1:50) for 40 min at 4°C. Cells were
776 washed twice with staining buffer and resuspended in 100 µl staining buffer. Data were

777 acquired on a BD FACS Canto II with high-throughput sampler using FACSDiva v9.2 (BD
778 Biosciences) with settings: flow rate 3.0, sample volume 50 µl, mixing volume 50 µl,
779 mixing speed 200, two washes with 200 µl wash volume. Analysis was performed using
780 FlowJo v10.10.

781 *Generating conditioned media from HPCs for chemotaxis study*

782 HPCs (3.5×10^5) were seeded into six-well plates coated with 20 µg/ml mouse laminin
783 (Sigma, Cat. No. L2020). After 24 h, media was replaced with proliferation media ± 1
784 ng/ml TNF-α. After 48 h, CM was collected and centrifuged at 1500 × g for 10 min at 4°C.
785 Supernatants were transferred to new tubes to remove cell debris and stored at –80°C
786 until use.

787 *Generating conditioned media from differentiating HPCs*

788 After 48 h of treatment in proliferation conditions as described above, media was replaced
789 with differentiation media ± 1 ng/ml TNF-α. Cells were differentiated for 7 days, with media
790 ± 1 ng/ml TNF-α refreshed every 48 h to simulate chronic inflammation. At the end of the
791 differentiation period, CM was collected, centrifuged at 1500 × g for 10 min at 4°C, and
792 the supernatants were transferred to new tubes and stored at –80°C for chemotaxis
793 assays.

794 *Generating conditioned media from HPCs blocking JAK activity or IFNAR*

795 3.5×10^5 HPCs were seeded in 6-well plates coated with 20 µg/ml mouse laminin
796 (Sigma, Cat. No. L2020). The following day, media was replaced with fresh proliferation
797 media with either DMSO (vehicle control), 1 ng/ml TNF-α, 10 µg/ml anifrolumab (anti-

IFNAR1; Bio X Cell, Cat. No. SIM0022) ± 1 ng/ml TNF-α, or 0.15 nM JAK inhibitor I (Cayman Chemical, Cat. No. CAY15146) ± 1 ng/ml TNF-α After 24 h, CM was collected, centrifuged at 1500 × g for 10 min at 4° C, and supernatants were transferred to fresh tubes and stored at −80° C for chemotaxis assays.

Data availability

All source data will be made available via the repository platform *figshare.com* and scripts on *github.com* at the same time as the peer-reviewed publication.

References

1. Ming, G. & Song, H. Adult Neurogenesis in the Mammalian Brain: Significant Answers and Significant Questions. *Neuron* **70**, 687–702 (2011).
2. Altman, J. Autoradiographic investigation of cell proliferation in the brains of rats and cats. *Anat Rec* **145**, 573–591 (1963).
3. Spalding, K. L. *et al.* Dynamics of Hippocampal Neurogenesis in Adult Humans. *Cell* **153**, 1219–1227 (2013).
4. Boldrini, M. *et al.* Human Hippocampal Neurogenesis Persists throughout Aging. *Cell Stem Cell* **22**, 589-599.e5 (2018).
5. Knoth, R. *et al.* Murine features of neurogenesis in the human hippocampus across the lifespan from 0 to 100 years. *PLoS One* **5**, e8809 (2010).
6. Moreno-Jiménez, E. P. *et al.* Adult hippocampal neurogenesis is abundant in neurologically healthy subjects and drops sharply in patients with Alzheimer's disease. *Nat Med* **25**, 554–560 (2019).
7. Tobin, M. K. *et al.* Human Hippocampal Neurogenesis Persists in Aged Adults and Alzheimer's Disease Patients. *Cell Stem Cell* **24**, 974-982.e3 (2019).
8. Palmer, T. D. *et al.* Progenitor cells from human brain after death. *Nature* **411**, 42–43 (2001).
9. Zhou, Y. *et al.* Molecular landscapes of human hippocampal immature neurons across lifespan. *Nature* **607**, 527–533 (2022).
10. Dumitru, I. *et al.* Identification of proliferating neural progenitors in the adult human hippocampus. *Science* **389**, 58–63 (2025).
11. Shors, T. J. *et al.* Neurogenesis in the adult is involved in the formation of trace memories. *Nature* **410**, 372–376 (2001).
12. Freund, J. *et al.* Emergence of Individuality in Genetically Identical Mice. *Science* **340**, 756–759 (2013).

13. Alonso, M., Petit, A.-C. & Lledo, P.-M. The impact of adult neurogenesis on affective functions: of mice and men. *Mol Psychiatry* **29**, 2527–2542 (2024).
14. Babcock, K. R., Page, J. S., Fallon, J. R. & Webb, A. E. Adult Hippocampal Neurogenesis in Aging and Alzheimer's Disease. *Stem Cell Reports* **16**, 681–693 (2021).
15. Berger, T., Lee, H., Young, A. H., Aarsland, D. & Thuret, S. Adult Hippocampal Neurogenesis in Major Depressive Disorder and Alzheimer's Disease. *Trends Mol Med* **26**, 803–818 (2020).
16. Hill, A. S., Sahay, A. & Hen, R. Increasing Adult Hippocampal Neurogenesis is Sufficient to Reduce Anxiety and Depression-Like Behaviors. *Neuropsychopharmacology* **40**, 2368–2378 (2015).
17. Li, Y.-D. *et al.* Activation of hypothalamic-enhanced adult-born neurons restores cognitive and affective function in Alzheimer's disease. *Cell Stem Cell* **30**, 415-432.e6 (2023).
18. Heneka, M. T. *et al.* Neuroinflammation in Alzheimer disease. *Nat Rev Immunol* **25**, 321–352 (2025).
19. Zhang, W., Sun, H.-S., Wang, X., Dumont, A. S. & Liu, Q. Cellular senescence, DNA damage, and neuroinflammation in the aging brain. *Trends Neurosci* **47**, 461–474 (2024).
20. Beurel, E., Toups, M. & Nemeroff, C. B. The Bidirectional Relationship of Depression and Inflammation: Double Trouble. *Neuron* **107**, 234–256 (2020).
21. Swardfager, W. *et al.* A Meta-Analysis of Cytokines in Alzheimer's Disease. *Biol Psychiatry* **68**, 930–941 (2010).
22. Holmes, C. *et al.* Systemic inflammation and disease progression in Alzheimer disease. *Neurology* **73**, 768–774 (2009).
23. Brymer, K. J., Romay-Tallon, R., Allen, J., Caruncho, H. J. & Kalynchuk, L. E. Exploring the Potential Antidepressant Mechanisms of TNFα Antagonists. *Front Neurosci* **13**, (2019).
24. Enache, D., Pariante, C. M. & Mondelli, V. Markers of central inflammation in major depressive disorder: A systematic review and meta-analysis of studies examining cerebrospinal fluid, positron emission tomography and post-mortem brain tissue. *Brain Behav Immun* **81**, 24–40 (2019).
25. Borsini, A., Zunszain, P. A., Thuret, S. & Pariante, C. M. The role of inflammatory cytokines as key modulators of neurogenesis. *Trends Neurosci* **38**, 145–57 (2015).
26. Monje, M. L., Toda, H. & Palmer, T. D. Inflammatory Blockade Restores Adult Hippocampal Neurogenesis. *Science* **302**, 1760–1765 (2003).
27. Chen, M., Reed, R. R. & Lane, A. P. Chronic Inflammation Directs an Olfactory Stem Cell Functional Switch from Neuroregeneration to Immune Defense. *Cell Stem Cell* **25**, 501-513.e5 (2019).
28. Dulken, B. W. *et al.* Single-cell analysis reveals T cell infiltration in old neurogenic niches. *Nature* **571**, 205–210 (2019).
29. Wu, Y. *et al.* Multimodal transcriptomics reveal neurogenic aging trajectories and age-related regional inflammation in the dentate gyrus. *Nat Neurosci* **28**, 415–430 (2025).

30. Laurent, C. *et al.* Hippocampal T cell infiltration promotes neuroinflammation and cognitive decline in a mouse model of tauopathy. *Brain* **140**, 184–200 (2017).
31. Walgrave, H. *et al.* Restoring miR-132 expression rescues adult hippocampal neurogenesis and memory deficits in Alzheimer's disease. *Cell Stem Cell* **28**, 1805-1821.e8 (2021).
32. Borsini, A. *et al.* Neurogenesis is disrupted in human hippocampal progenitor cells upon exposure to serum samples from hospitalized COVID-19 patients with neurological symptoms. *Mol Psychiatry* **27**, 5049–5061 (2022).
33. Du Preez, A. *et al.* The serum metabolome mediates the concert of diet, exercise, and neurogenesis, determining the risk for cognitive decline and dementia. *Alzheimer's & Dementia* **18**, 654–675 (2022).
34. Maruszak, A. *et al.* Predicting progression to Alzheimer's disease with human hippocampal progenitors exposed to serum. *Brain* **146**, 2045–2058 (2023).
35. Anacker, C. *et al.* Role for the kinase SGK1 in stress, depression, and glucocorticoid effects on hippocampal neurogenesis. *Proceedings of the National Academy of Sciences* **110**, 8708–8713 (2013).
36. de Lucia, C. *et al.* Lifestyle mediates the role of nutrient-sensing pathways in cognitive aging: cellular and epidemiological evidence. *Commun Biol* **3**, 157 (2020).
37. Gutierrez, H. & Davies, A. M. Regulation of neural process growth, elaboration and structural plasticity by NF-κB. *Trends Neurosci* **34**, 316–325 (2011).
38. Carvajal Ibañez, D. *et al.* Interferon regulates neural stem cell function at all ages by orchestrating mTOR and cell cycle. *EMBO Mol Med* **15**, (2023).
39. Borsini, A. *et al.* Interferon-Alpha Reduces Human Hippocampal Neurogenesis and Increases Apoptosis via Activation of Distinct STAT1-Dependent Mechanisms. *Int J Neuropsychopharmacol* **21**, 187–200 (2018).
40. Yarilina, A., Park-Min, K.-H., Antoniv, T., Hu, X. & Ivashkiv, L. B. TNF activates an IRF1-dependent autocrine loop leading to sustained expression of chemokines and STAT1-dependent type I interferon–response genes. *Nat Immunol* **9**, 378–387 (2008).
41. Venkatesh, D. *et al.* Endothelial TNF Receptor 2 Induces IRF1 Transcription Factor-Dependent Interferon-β Autocrine Signaling to Promote Monocyte Recruitment. *Immunity* **38**, 1025–1037 (2013).
42. Bonelli, M. *et al.* IRF1 is critical for the TNF-driven interferon response in rheumatoid fibroblast-like synoviocytes. *Exp Mol Med* **51**, 1–11 (2019).
43. Riggs, J. M. *et al.* Characterisation of anifrolumab, a fully human anti-interferon receptor antagonist antibody for the treatment of systemic lupus erythematosus. *Lupus Sci Med* **5**, e000261 (2018).
44. Thompson, J. E. *et al.* Photochemical preparation of a pyridone containing tetracycle: A jak protein kinase inhibitor. *Bioorg Med Chem Lett* **12**, 1219–1223 (2002).
45. Chauquet, S. *et al.* Exercise rejuvenates microglia and reverses T cell accumulation in the aged female mouse brain. *Aging Cell* **23** (2024).
46. Krukowski, K. *et al.* Small molecule cognitive enhancer reverses age-related memory decline in mice. *Elife* **9**, (2020).

47. Unger, M. S. *et al.* CD8+ T-cells infiltrate Alzheimer's disease brains and regulate neuronal- and synapse-related gene expression in APP-PS1 transgenic mice. *Brain Behav Immun* **89**, 67–86 (2020).
48. Gate, D. *et al.* Clonally expanded CD8 T cells patrol the cerebrospinal fluid in Alzheimer's disease. *Nature* **577**, 399–404 (2020).
49. Merlini, M., Kirabali, T., Kulic, L., Nitsch, R. M. & Ferretti, M. T. Extravascular CD3+ T Cells in Brains of Alzheimer Disease Patients Correlate with Tau but Not with Amyloid Pathology: An Immunohistochemical Study. *Neurodegener Dis* **18**, 49–56 (2018).
50. Groom, J. R. & Luster, A. D. CXCR3 ligands: redundant, collaborative and antagonistic functions. *Immunol Cell Biol* **89**, 207–215 (2011).
51. Hsu, W.-L., Ma, Y.-L., Hsieh, D.-Y., Liu, Y.-C. & Lee, E. H. STAT1 Negatively Regulates Spatial Memory Formation and Mediates the Memory-Impairing Effect of Aβ. *Neuropsychopharmacology* **39**, 746–758 (2014).
52. Imitola, J. *et al.* Stat1 is an inducible transcriptional repressor of neural stem cells self-renewal program during neuroinflammation. *Front Cell Neurosci* **17**, (2023).
53. Zheng, L.-S. *et al.* Mechanisms for Interferon-α-Induced Depression and Neural Stem Cell Dysfunction. *Stem Cell Reports* **3**, 73–84 (2014).
54. Baruch, K. *et al.* Aging-induced type I interferon response at the choroid plexus negatively affects brain function. *Science* **346**, 89–93 (2014).
55. Chen, Z. & Palmer, T. D. Differential roles of TNFR1 and TNFR2 signaling in adult hippocampal neurogenesis. *Brain Behav Immun* **30**, 45–53 (2013).
56. Liu, Y.-P., Lin, H.-I. & Tzeng, S.-F. Tumor necrosis factor-α and interleukin-18 modulate neuronal cell fate in embryonic neural progenitor culture. *Brain Res* **1054**, 152–158 (2005).
57. Keohane, A., Ryan, S., Maloney, E., Sullivan, A. M. & Nolan, Y. M. Tumour necrosis factor-α impairs neuronal differentiation but not proliferation of hippocampal neural precursor cells: Role of Hes1. *Molecular and Cellular Neuroscience* **43**, 127–135 (2010).
58. Neumann, H. *et al.* Tumor Necrosis Factor Inhibits Neurite Outgrowth and Branching of Hippocampal Neurons by a Rho-Dependent Mechanism. *The Journal of Neuroscience* **22**, 854–862 (2002).
59. Sheng, W. S. *et al.* TNF-α-induced chemokine production and apoptosis in human neural precursor cells. *J Leukoc Biol* **78**, 1233–1241 (2005).
60. McNab, F., Mayer-Barber, K., Sher, A., Wack, A. & O'Garra, A. Type I interferons in infectious disease. *Nat Rev Immunol* **15**, 87–103 (2015).
61. Ninh, V. K. *et al.* Spatially clustered type I interferon responses at injury borderzones. *Nature* **633**, 174–181 (2024).
62. Ashby, K. M. *et al.* Sterile production of interferons in the thymus affects T cell repertoire selection. *Sci Immunol* **9**, (2024).
63. Tliba, O. *et al.* Tumor Necrosis Factor α Modulates Airway Smooth Muscle Function via the Autocrine Action of Interferon β. *Journal of Biological Chemistry* **278**, 50615–50623 (2003).
64. Escoubas, C. C. *et al.* Type I interferon responsive microglia shape cortical development and behavior. Preprint at https://doi.org/10.1101/2021.04.29.441889 (2021).

65. de Weerd, N. A. & Nguyen, T. The interferons and their receptors—distribution and regulation. *Immunol Cell Biol* **90**, 483–491 (2012).
66. Deczkowska, A. *et al.* Mef2C restrains microglial inflammatory response and is lost in brain ageing in an IFN-I-dependent manner. *Nat Commun* **8**, 717 (2017).
67. Roy, E. R. *et al.* Type I interferon response drives neuroinflammation and synapse loss in Alzheimer disease. *Journal of Clinical Investigation* **130**, 1912–1930 (2020).
68. Roy, E. R. *et al.* Concerted type I interferon signaling in microglia and neural cells promotes memory impairment associated with amyloid β plaques. *Immunity* **55**, 879-894.e6 (2022).
69. Licht-Murava, A. *et al.* Astrocytic TDP-43 dysregulation impairs memory by modulating antiviral pathways and interferon-inducible chemokines. *Sci Adv* **9**, (2023).
70. Wang, Q. *et al.* Brain derived β-interferon is a potential player in Alzheimer's disease pathogenesis and cognitive impairment. *Alzheimers Res Ther* **16**, 271 (2024).
71. Hur, J.-Y. *et al.* The innate immunity protein IFITM3 modulates γ-secretase in Alzheimer's disease. *Nature* **586**, 735–740 (2020).
72. Stokes, C. *et al.* The human neural cell atlas of Zika virus infection in developing brain tissue. *Cell Rep Med* **6**, 102189 (2025).
73. Fernando, N. *et al.* Single-cell multiomic analysis reveals the involvement of Type I interferon-responsive CD8+ T cells in amyloid beta-associated memory loss. Preprint at https://doi.org/10.1101/2023.03.18.533293 (2023).
74. Mason, H. D. & McGavern, D. B. How the immune system shapes neurodegenerative diseases. *Trends Neurosci* **45**, 733–748 (2022).
75. Chen, X. & Holtzman, D. M. Emerging roles of innate and adaptive immunity in Alzheimer's disease. *Immunity* **55**, 2236–2254 (2022).
76. Groh, J. *et al.* Microglia activation orchestrates CXCL10-mediated CD8+ T cell recruitment to promote aging-related white matter degeneration. *Nat Neurosci* **28**, 1160–1173 (2025).
77. Ma, W. *et al.* Type I interferon response in astrocytes promotes brain metastasis by enhancing monocytic myeloid cell recruitment. *Nat Commun* **14**, 2632 (2023).
78. Nelson, T. E. & Gruol, D. L. The chemokine CXCL10 modulates excitatory activity and intracellular calcium signaling in cultured hippocampal neurons. *J Neuroimmunol* **156**, 74–87 (2004).
79. Petrisko, T. J. *et al.* Neuronal CXCL10/CXCR3 Axis Mediates the Induction of Cerebral Hyperexcitability by Peripheral Viral Challenge. *Front Neurosci* **14**, (2020).
80. Kalamakis, G. *et al.* Quiescence Modulates Stem Cell Maintenance and Regenerative Capacity in the Aging Brain. *Cell* **176**, 1407-1419.e14 (2019).
81. Du Preez, A. *et al.* Impaired hippocampal neurogenesis in vitro is modulated by dietary-related endogenous factors and associated with depression in a longitudinal ageing cohort study. *Mol Psychiatry* **27**, 3425–3440 (2022).
82. Farmand, S., Ahmed, E., Zawar, H. A. & Thuret, S. Selenium deficiency negatively affects survival and integrity of human hippocampal progenitor cells. *Aging Brain* **7**, 100138 (2025).

83. Wu, T. *et al.* clusterProfiler 4.0: A universal enrichment tool for interpreting omics data. *The Innovation* **2**, 100141 (2021).
84. Badia-I-Mompel, P. *et al.* decoupleR: ensemble of computational methods to infer biological activities from omics data. *Bioinformatics advances* **2**, vbac016 (2022).
85. Müller-Dott, S. *et al.* Expanding the coverage of regulons from high-confidence prior knowledge for accurate estimation of transcription factor activities. *Nucleic Acids Res* **51**, 10934–10949 (2023).
86. Türei, D. *et al.* Integrated intra- and intercellular signaling knowledge for multicellular omics analysis. *Mol Syst Biol* **17**, (2021).

Authors contribution

L.S.K. and S.T. contributed equally and directed the research. T.A.D.N., L.S.K., and S.T. designed the experiments. T.A.D.N. wrote the manuscript with contributions from L.S.K. T.A.D.N. performed the majority of the experiments and conducted data analysis. T.A.D.N. and D.T.R. generated the scRNA sequencing data in collaboration. A.B. collected and analysed the RT-qPCR data. S.S. performed the morphological analysis of differentiated HPCs. H.L. helped design and generate the differentiation and chemokine data. T.A.D.N. and L.A.O'N. generated the ELISA and chemokine data. S.J. advised on STAT signalling and helped generate the STAT western blot data. All authors read and revised the manuscript.

Acknowledgements

T.A.D.N. was funded by the Wellcome Trust as part of the "Neuro-Immune Interactions in Health & Disease Wellcome Trust PhD Programme [218452/Z/19/Z]". The work was supported by a grant awarded to S.T. by the Medical Research Council UK [MR/S00484X/1] and awards to L.S.K. by the Medical Research Council Discovery

Award [MR/N012345/1]. D.T.R. was supported by a PhD Studentship awarded by the Medical Research Council UK [MR/R015643/1], H.L. was supported by a grant from The Galen and Hilary Weston Foundation awarded to S.T. Some panels of Figure 5 and 6 were created with Biorender.com with a licence to S.T. at King's College London.

We thank George Chennell and Chen Liang (Wohl Cellular Imaging Centre, King's College London) for technical support with high-content imaging; the Genomics Research Platform (Guy's and St Thomas' NHS Foundation Trust) for sequencing support; Franziska Denk for advice on scRNA sequencing design; Robert Köchl and Aritz Lasarte Cía for input on chemotaxis assays; Josephine Eum for guidance on PBMC isolation; and Daniel Davies for advice on flow cytometry staining.

Ethics declaration

The authors declare that ethical standards prevailing at their institution have been observed throughout this study.

Competing interests

The authors declare no competing interests.

Extended data p. 2-6

&

Supplementary Information p.7-24

TNF-α-induced type I IFN signalling decreases neurogenesis and drives T cell chemotaxis

Tinne Amalie Damgaard Nissen[1,2], Arishma Baig[1], Daniel T. Rock[2], Sandra Shibu[2], Hyunah Lee[2], Lauren A. O'Neill[1], Susan John[3], Linda S. Klavinskis[1]*, Sandrine Thuret[2]*

[1]Department of Infectious Diseases, School of Immunology & Microbial Sciences, King's College London, London SE1 9RT, UK
[2]Department of Basic and Clinical Neuroscience, Institute of Psychiatry, Psychology and Neuroscience, King's College London, London SE5 9RT, UK
[3]Peter Gorer Department of Immunobiology, King's College London, London SE1 9RT, UK

*Equally contributed and co-corresponding authors. Linda.Klavinskis@kcl.ac.uk and Sandrine.1.thuret@kcl.ac.uk

Extended data

TNF-α-induced type I IFN signalling decreases neurogenesis and drives T cell chemotaxis

Tinne Amalie Damgaard Nissen[1,2], Arishma Baig[1], Daniel T. Rock[2], Sandra Shibu[2], Hyunah Lee[2], Lauren A. O'Neill[1], Susan John[3], Linda S. Klavinskis[1]*, Sandrine Thuret[2]*

[1]Department of Infectious Diseases, School of Immunology & Microbial Sciences, King's College London, London SE1 9RT, UK
[2]Department of Basic and Clinical Neuroscience, Institute of Psychiatry, Psychology and Neuroscience, King's College London, London SE5 9RT, UK
[3]Peter Gorer Department of Immunobiology, King's College London, London SE1 9RT, UK

*Equally contributed and co-corresponding authors. Linda.Klavinskis@kcl.ac.uk and Sandrine.1.thuret@kcl.ac.uk

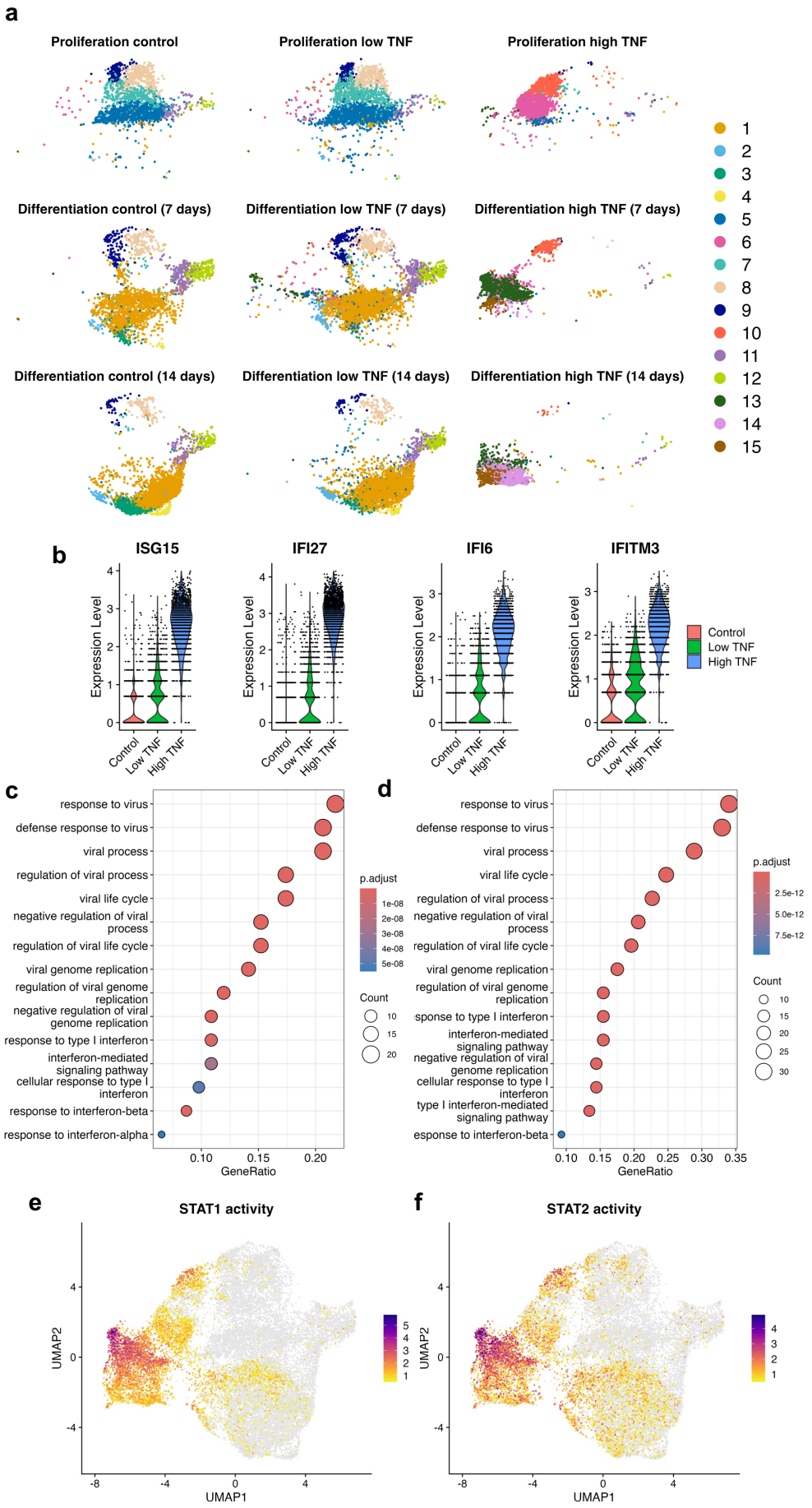
a
Proliferation control
Proliferation low TNF
Proliferation high TNF
Differentiation control (7 days)
Differentiation low TNF (7 days)
Differentiation high TNF (7 days)
Differentiation control (14 days)
Differentiation low TNF (14 days)
Differentiation high TNF (14 days)
1
2
3
4
5
6
7
8
9
10
11
12
13
14
15
b
ISG15
IFI27
IFI6
IFITM3
Expression Level
Control
Low TNF
High TNF
c
response to virus
defense response to virus
viral process
regulation of viral process
viral life cycle
negative regulation of viral process
regulation of viral life cycle
viral genome replication
regulation of viral genome replication
negative regulation of viral genome replication
response to type I interferon
interferon-mediated signaling pathway
cellular response to type I interferon
response to interferon-beta
response to interferon-alpha
GeneRatio
p.adjust
Count
d
response to virus
defense response to virus
viral process
viral life cycle
regulation of viral process
negative regulation of viral process
regulation of viral life cycle
viral genome replication
regulation of viral genome replication
sponse to type I interferon
interferon-mediated signaling pathway
negative regulation of viral genome replication
cellular response to type I interferon
type I interferon-mediated signaling pathway
esponse to interferon-beta
GeneRatio
p.adjust
Count
e
STAT1 activity
UMAP2
UMAP1
f
STAT2 activity
UMAP2
UMAP1

Extended Fig. 1 | TNF-α drives the upregulation of type I IFN genes in HPCs. a, UMAP plot showing transcriptional clustering of single cells split by samples. Colours indicate the 15 cell clusters identified. **b**, Violin plots showing dose-dependent expression of the type I IFN stimulated genes ISG15, IFI27, IFI6, and IFITM3 in the HPCs treated for 48 hrs with vehicle (red), 0.1 ng/ml (low, green), or 1 ng/ml (high, blue) TNF-α. **c**, Dot plot showing gene ontology (GO) enrichment analysis of biological processes terms based on the top 100 genes upregulated genes in cluster 5 as compared to cluster 6. **d**, Dot plot showing gene ontology (GO) enrichment analysis of biological processes terms based on the top 100 genes upregulated genes in cluster 10 as compared to cluster 7, 8, and 9. **e**, UMAP plot showing the predicted transcription factor activity of STAT1. **f**, UMAP plot showing the predicted transcription factor activity of STAT2.

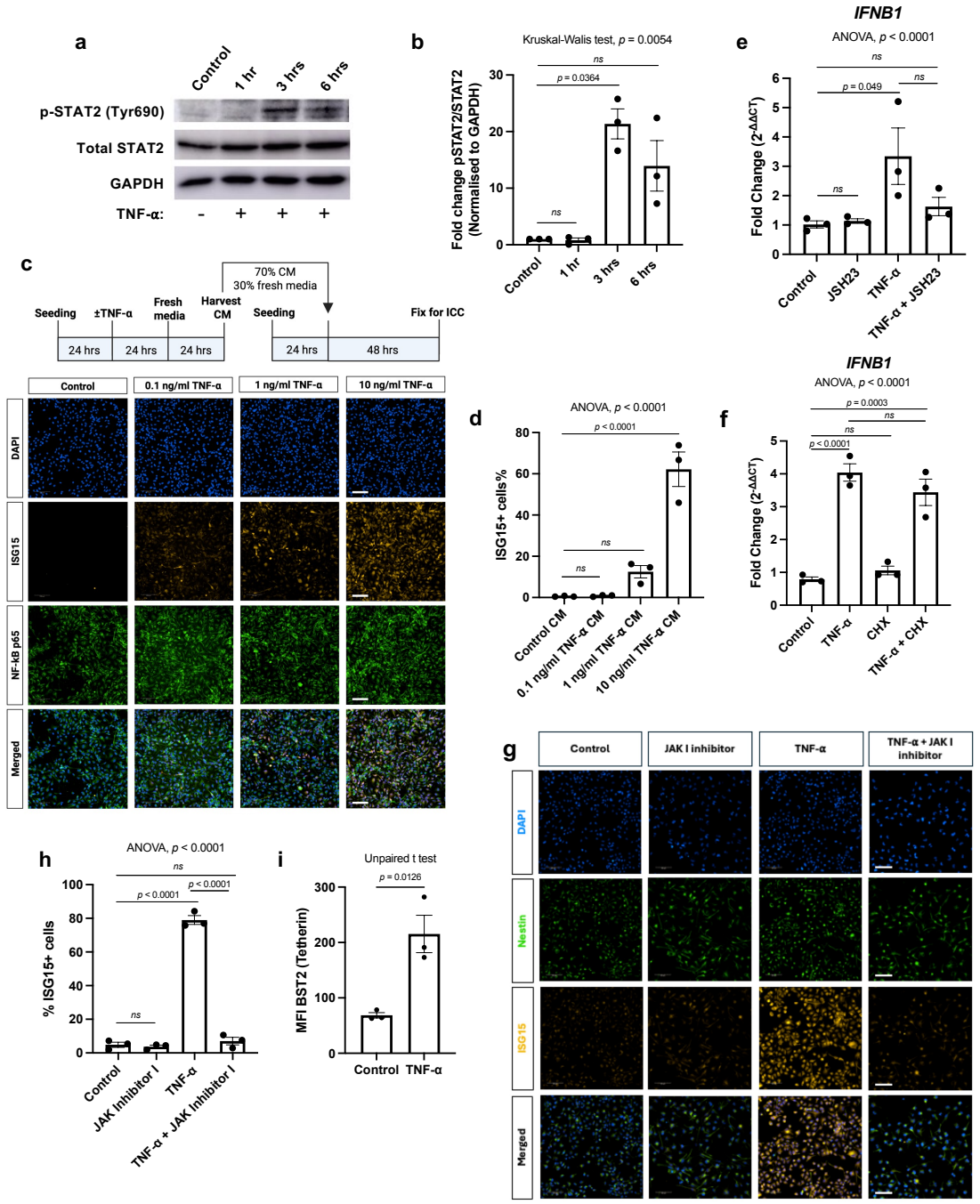

Extended Fig. 2 | TNF-α drives type I IFN signalling in human HPCs via autocrine/paracrine signalling via IFNAR. **a**, Representative western blots of three independent experiments showing the activation of STAT2 in HPCs treated with 1 ng/ml TNF-α for 1 h, 3 h, 6 h or 12 h. Cell lysates were probed for phosphorylated STAT2 (p-STAT2, Tyr690), total STAT2, and GAPDH as a loading control. **b**, Quantification of STAT2 activation in human hippocampal progenitor cells from A. pSTAT2 and STAT2 intensities were normalised to GAPDH intensity before calculating the fold change pSTAT2/STAT2 relative to control. Data represent mean ± SEM from three independent experiments. Statistical analysis: Kruskal-Wallis test followed by Dunn's post hoc correction. **c**, Representative images of three

independent experiments with similar results showing the expression of ISG15 (orange) on HPCs. Scale bar = 100 μm. HPCs treated for 48 hrs with conditioned media (CM) from other HPCs treated ± TNF-α for 24 hrs followed by 24 hrs treatment with media. **d**, Quantification of the percentage of ISG15+ cells based on C. Data represent mean ± SEM. Statistical analysis: one-way ANOVA followed by Bonferroni's multiple comparisons test. **e**, RT-qPCR data showing the relative gene expression of *IFNB1* in HPCs pre-treated with 10 μM JSH23 or DMSO, followed by three hours of treatment ± 1 ng/ml TNF-α. Data represent as mean ± SEM of three independent experiments. Statistical analysis: one-way ANOVA followed by Bonferroni's multiple comparisons test. **f**, RT-qPCR data showing the relative gene expression of *IFNB1* in HPCs pre-treated with 10 μg/ml cycloheximide (CHX) or DMSO followed by three hours of treatment ± 1 ng/ml TNF-α. Data represent as mean ± SEM of three independent experiments. Statistical analysis: one-way ANOVA followed by Bonferroni's multiple comparisons test. **g**, Representative images of three independent experiments with similar results showing the expression of ISG15 (orange) on HPCs. Scale bar = 100 μm. HPCs were treated for 24 hrs with 16 nM JAK inhibitor I or DMSO, ± 1 ng/ml TNF-α. **h**, Quantification of the percentage of ISG15+ cells based on G. Data represent mean ± SEM. Statistical analysis: one-way ANOVA followed by Bonferroni's multiple comparisons test. **i**, Cell surface expression of IFN-regulated BST2 (tetherin) quantified by measuring the mean fluorescence intensity (MFI) on HPCs treated 24 hrs ± 1 ng/ml TNF-α using flow cytometry. Data represent mean ± SEM. Statistical analysis: unpaired t-test.

Supplementary Information

TNF-α-induced type I IFN signalling decreases neurogenesis and drives T cell chemotaxis

Tinne Amalie Damgaard Nissen[1,2], Arishma Baig[1], Daniel T. Rock[2], Sandra Shibu[2], Hyunah Lee[2], Lauren A. O'Neill[1], Susan John[3], Linda S. Klavinskis[1]*, Sandrine Thuret[2]*

[1]Department of Infectious Diseases, School of Immunology & Microbial Sciences, King's College London, London SE1 9RT, UK
[2]Department of Basic and Clinical Neuroscience, Institute of Psychiatry, Psychology and Neuroscience, King's College London, London SE5 9RT, UK
[3]Peter Gorer Department of Immunobiology, King's College London, London SE1 9RT, UK

*Equally contributed and co-corresponding authors. Linda.Klavinskis@kcl.ac.uk and Sandrine.1.thuret@kcl.ac.uk

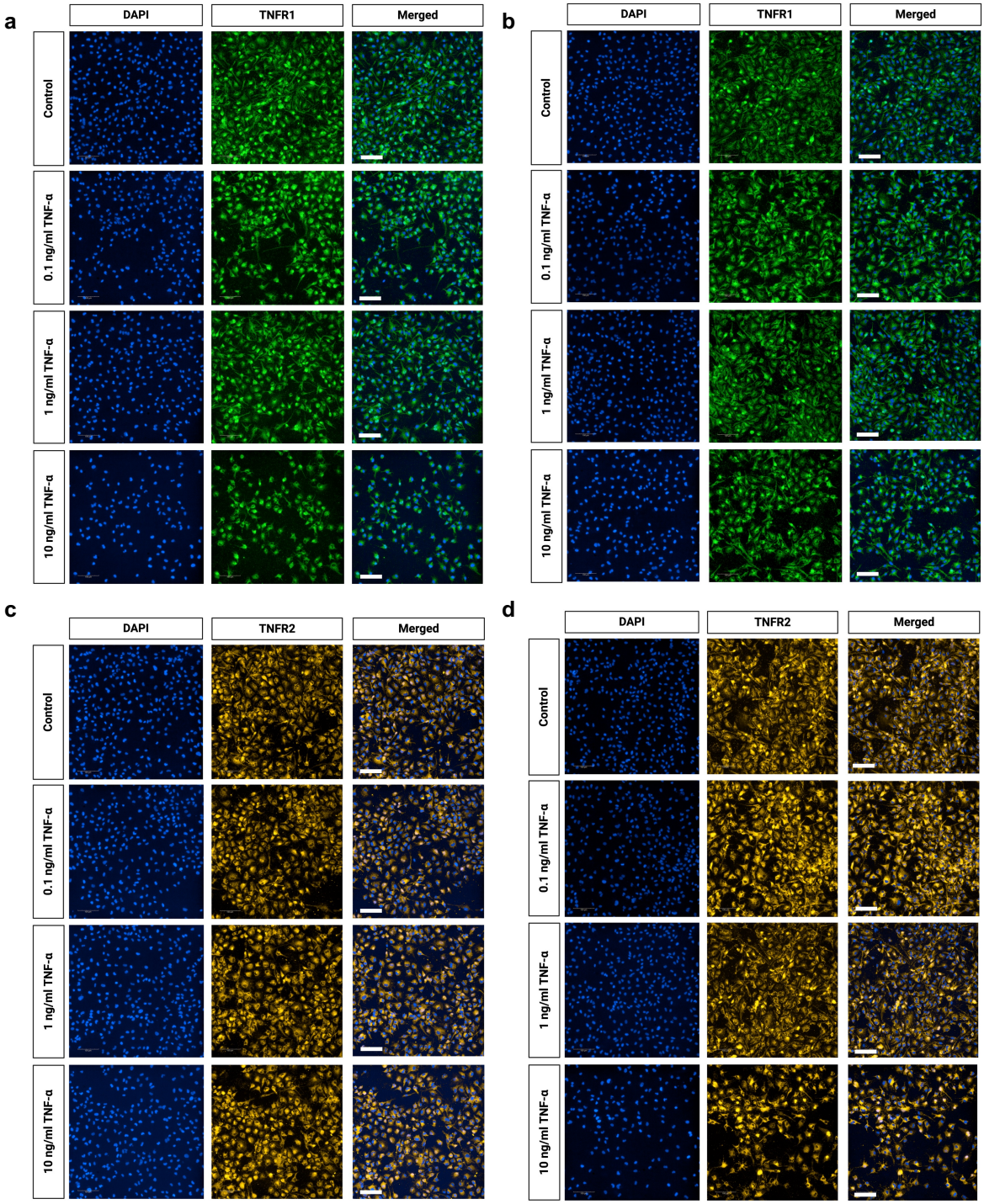

Supplementary Fig. 1 | TNFR expression on human HPCs treated ± TNF-α. a, and **b** Representative images of three independent experiments with similar results showing the expression of TNFR1 (green) on HPCs treated ± TNF-α for **a** 24 h or **b** 48 h. **c** and **d** Representative images of three independent experiments with similar results showing the expression of TNFR2 (orange) on HPCs treated ± TNF-α for **c** 24 h or **d** 48 h. Scale bar = 100 μm. DAPI; 4′,6-diamidino-2-phenylindole, HPC; hippocampal progenitor cells, TNFR1; tumour necrosis factor receptor 1.

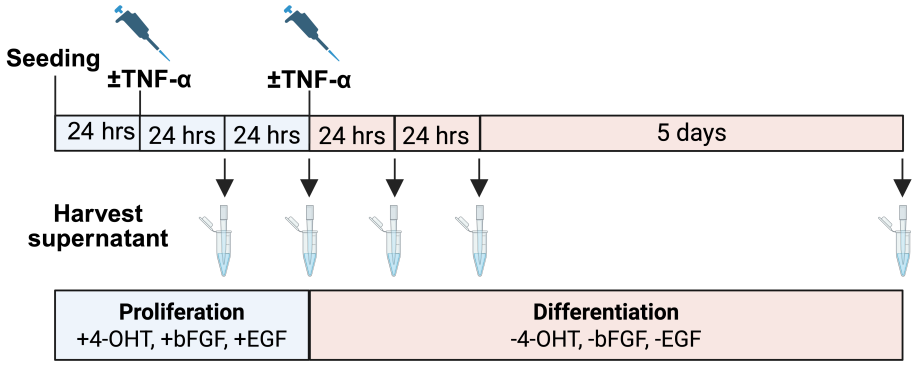

Supplementary Fig. 2 | Schematic overview of the experimental design for harvesting supernatant from HPCs and their differentiated progeny. The day following seeding, the proliferating HPCs were treated ± TNF-α (0.1 ng/ml, 1 ng/ml, or 10 ng/ml). After 24 h, the supernatant was harvested. After 48 h of treatment, the supernatant was harvested, and the media was changed to induce differentiation (removal of 4-OHT, bFGF, and EGF) ± TNF-α (0.1 ng/ml, 1 ng/ml, or 10 ng/ml). The supernatant of the differentiating cells was harvested after 24 h, 48 h, or 7 days of differentiation. 4-OHT; 4- hydroxytamoxifen, bFGF; basic fibroblast growth factor, EGF; epidermal growth factor.

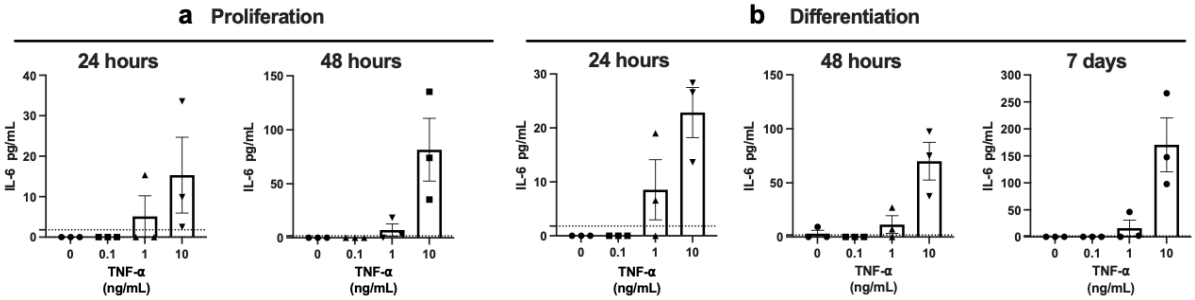

Supplementary Fig. 3 | ELISA measurement of IL-6 in the supernatant of HPCs and their differentiated progeny treated with TNF-α. a, Concentrations of IL-6 in the supernatant of proliferating HPCs 24 h and 48 h after TNF-α treatment. **b,** IL-6 in the supernatant of differentiating HPCs 24 h, 48 h, and 7 days after TNF-α treatment. Data is presented as mean ± SEM of three independent experiments.

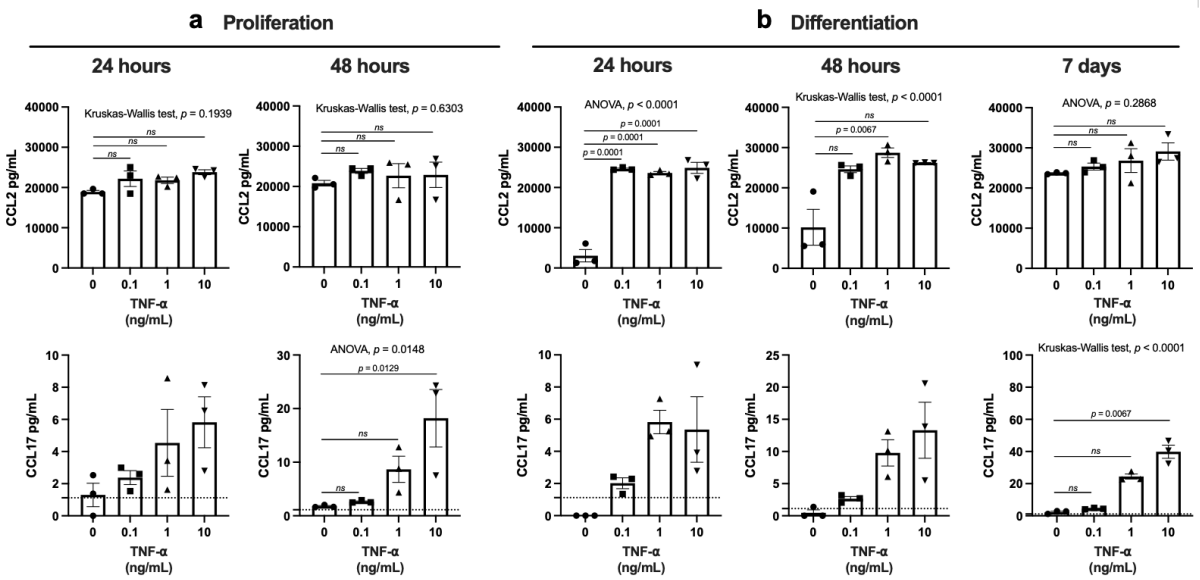

Supplementary Fig. 4 | CCL2 and CCL17 levels in the supernatant of HPCs and their differentiated progeny treated with TNF-α. a, Concentrations of CCL2 (upper panel) and CCL17 (lower panel) in the supernatant of proliferating HPCs 24 h and 48 h after TNF-α treatment. **b,** CCL2 (upper panel) and CCL17 (lower panel) in the supernatant of differentiating HPCs 24 h, 48 h, and 7 days after TNF-α treatment. Data is presented as mean ± SEM of three independent experiments. Statistical test: Kruskal-Wallis test followed by Dunn's post hoc correction, or one-way ANOVA followed by Bonferroni's multiple comparisons, as indicated above the graphs. Dashed lines mark the detection limit for CCL17 (1.12 pg/ml).

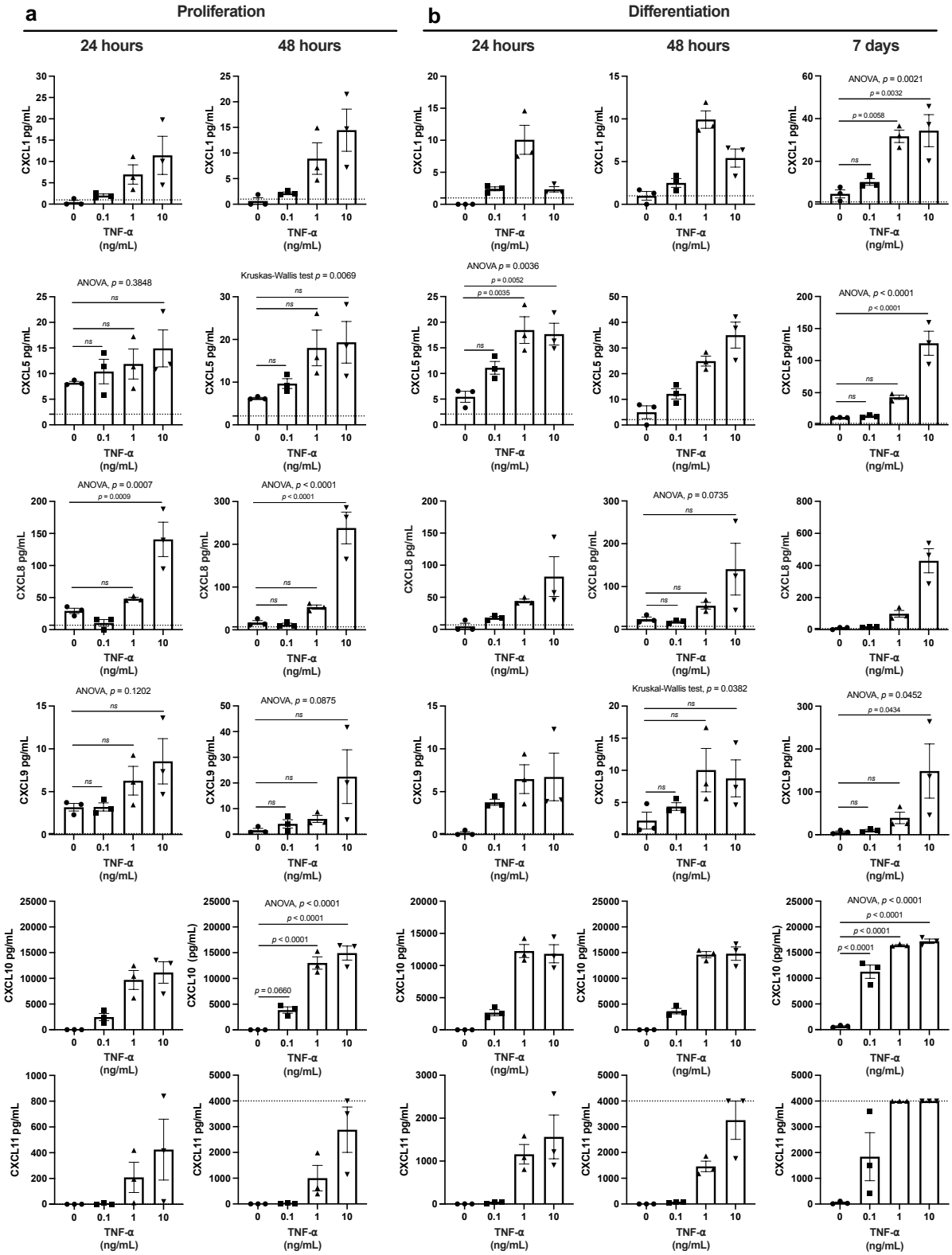

Supplementary Fig. 5 | CXC chemokine levels in the supernatant of HPCs and their differentiated progeny treated with TNF-α. a, Concentrations of CXCL1, CXCL5, IL-8, CXCL9, CXCL10, and CXCL11 in the supernatant of proliferating HPCs 24 h and 48 h after TNF-α treatment. **b,** CXCL1, CXCL5, IL-8, CXCL9, CXCL10, and CXCL11 levels in the supernatant of differentiating HPCs 24 h, 48 h, and 7 days after TNF-α treatment. Data is

presented as mean ± SEM of three independent experiments. Statistical test: Kruskal-Wallis test followed by Dunn's post hoc correction or one-way ANOVA followed by Bonferroni's multiple comparisons as indicated above the graphs. Dashed lines mark the detection limits (lower limit for CXCL1: <0.99 pg/ml, lower limit for CXCL5: <2.07 pg/ml, lower limit for CXCL8: <6.86 pg/ml, lower limit for CXCL9: <0.098 pg/ml, lower limit for CXCL10: <23.44 pg/ml, lower limit for CXCL11 <2.13 pg/ml, and upper limit for CXCL11 > 4000 pg/ml). For visualisation, data points below the detection limit were set to zero, and data points above the upper detection limit for CXCL11 were set to the limit of 4000 pg/ml.

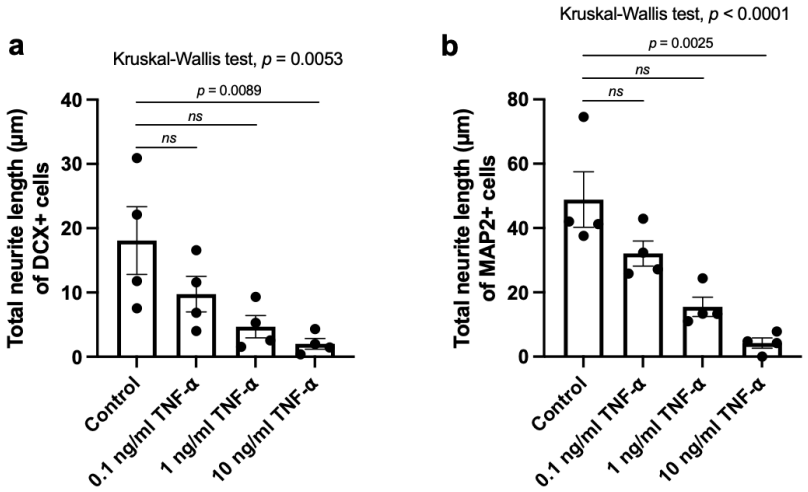

Supplementary Fig. 6 | Chronic TNF-α dose-dependently decreases the neurite length of DCX+ and MAP2+ differentiating HPCs. Quantification of the total neurite length (µm) of **a** DCX+ cells and **b** MAP2+ cells after seven days of differentiation ± chronic treatment with 0.1, 1, or 10 ng/ml TNF-α. Data represent mean ± SEM from four independent experiments. Statistical analysis: Kruskal-Wallis test followed by Dunn's post hoc correction**.**

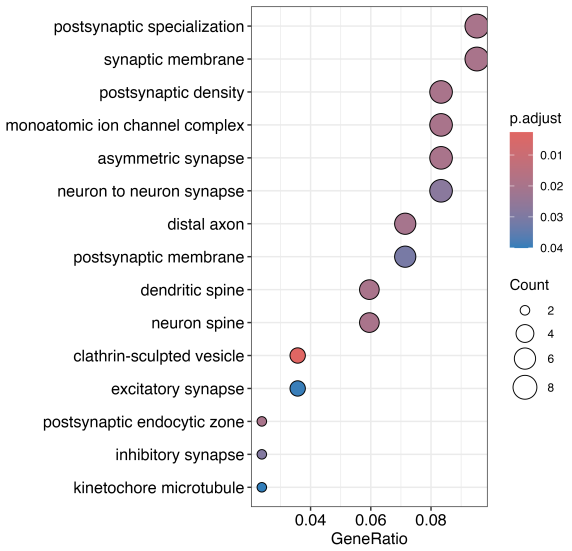

Supplementary Fig. 7 | Neuronal cellular components enriched in cluster 12. Dot plot showing GO cellular component enrichment based on the top 100 genes positively defining cluster 12.

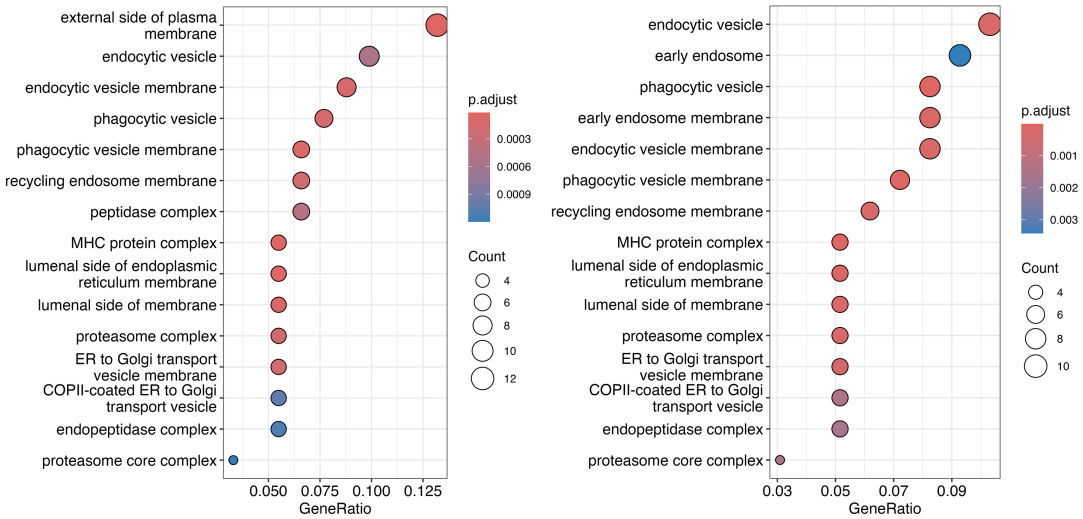

Supplementary Fig. 8 | Immune-related cellular components enriched in high-dose TNF-α-specific RGL-like and IPC-like clusters. Dot plot showing GO cellular component enrichment based on the top 100 genes upregulated in cluster 6 as compared to cluster 5 (left). Dot plot showing GO cellular component enrichment based on the top 100 genes upregulated genes in cluster 10 as compared to cluster 7, 8, and 9 (right).

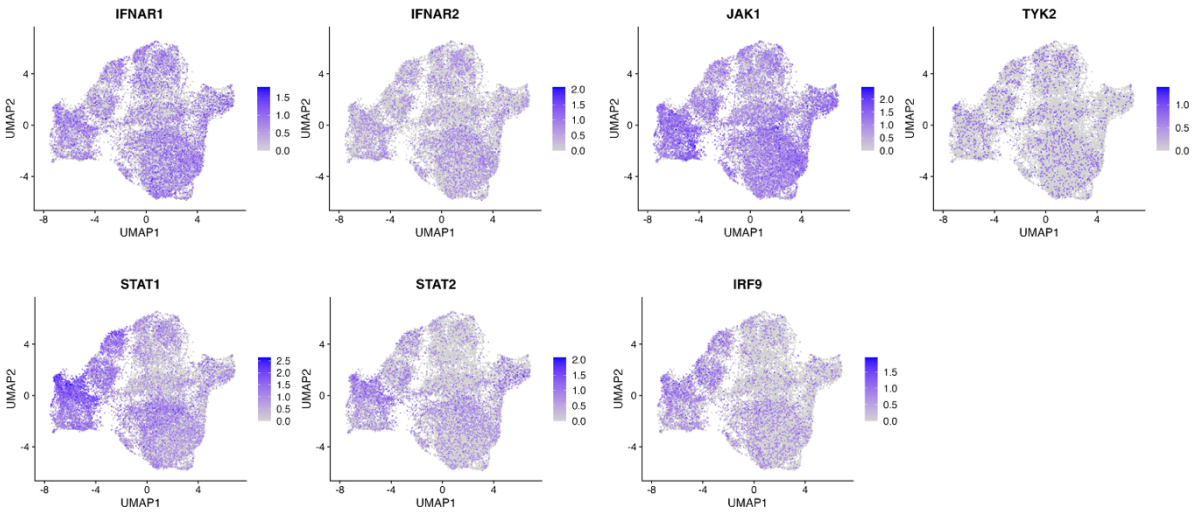

Supplementary Fig. 9 | Molecular machinery for type I interferon signalling. UMAP plots showing the expression of key genes required for type I interferon signalling: *IFNAR1*, *IFNAR2*, *JAK1*, *TYK2*, *STAT1*, *STAT2*, and *IRF9*.

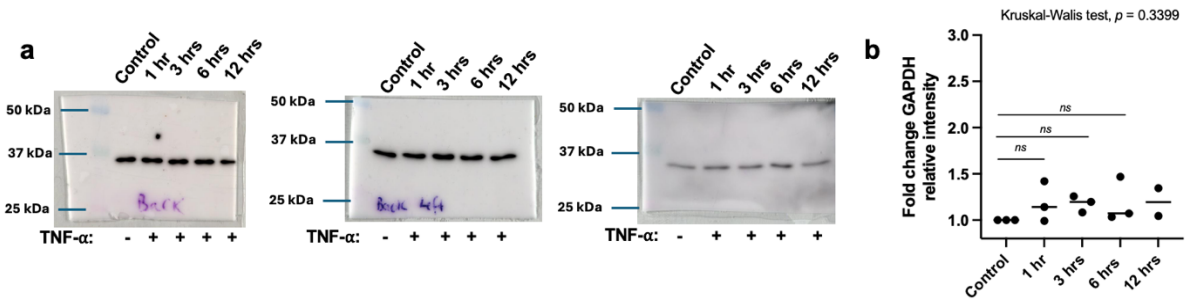

Supplementary Fig. 10 | TNF-α does not regulate GAPDH expression. a, Uncropped Western blot images for the three independent experiments probing for GAPDH. The HPCs were treated with 1 ng/ml TNF-α for 1, 3, 6, or 12 hours. Molecular weight markers (Precision Plus Protein Kaleidoscope Prestained Protein Standards) are shown for reference. **b,** Quantification of GAPDH band intensities in **a**. Data represent mean ± SEM. Statistical analysis: Kruskal-Wallis test followed by Dunn's post hoc correction**.**

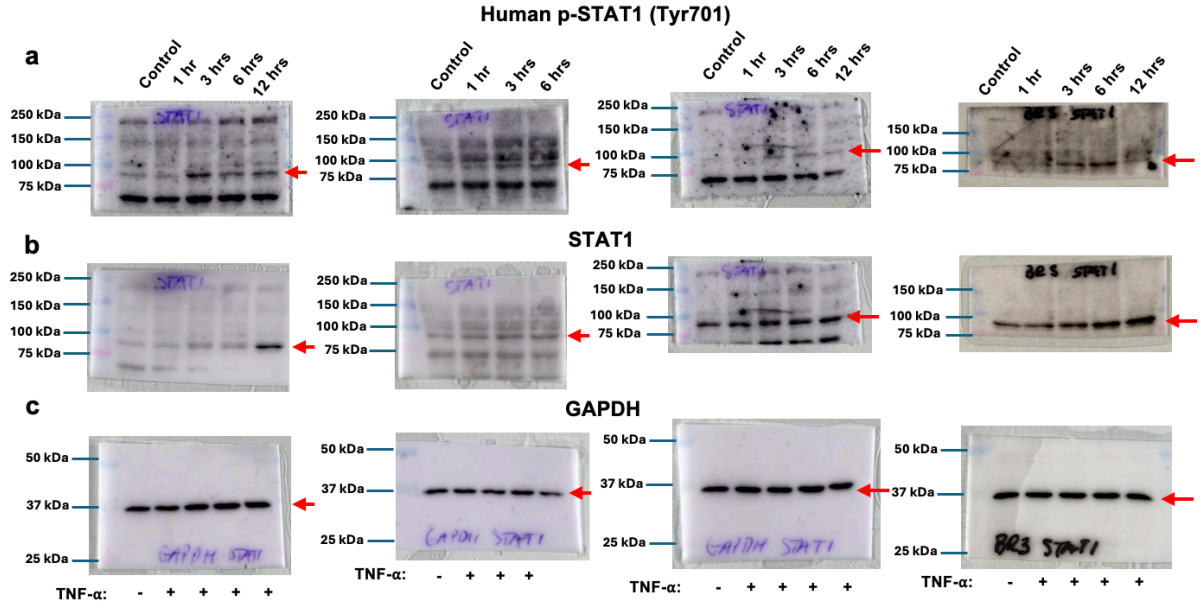

Supplementary Fig. 11 | Uncropped Western blots corresponding to Fig. 4a-b. a, Uncropped Western blot images from four independent experiments probing for pSTAT1 (Tyr701). **b,** Uncropped Western blot images from four independent experiments probing for total STAT1. **c,** Uncropped Western blot images from four independent experiments probing for loading control GAPDH. HPCs were treated with 1 ng/ml TNF-α for 1, 3, 6, or 12 hours. Molecular weight markers (Precision Plus Protein Kaleidoscope Prestained Protein Standards) are shown for reference. Red arrows indicate the bands of interest.

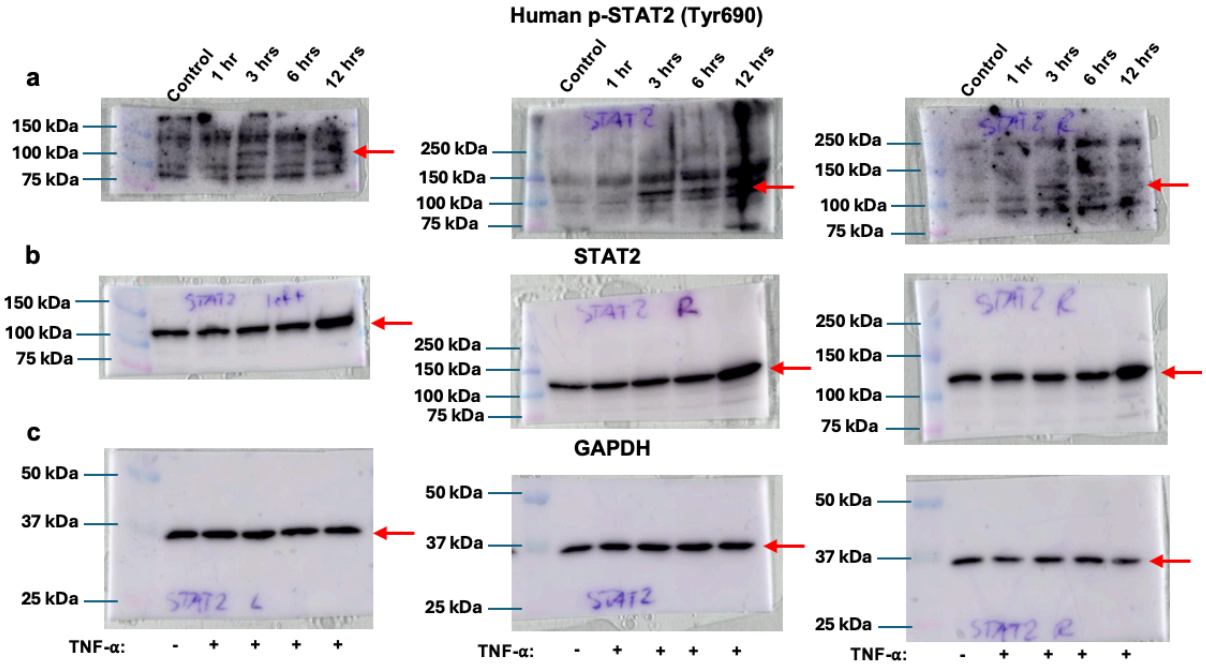

Supplementary Fig. 12 | Uncropped Western blots corresponding to Extended data Fig. 1a-b. a, Uncropped Western blot images from four independent experiments probing for pSTAT2 (Tyr690). **b,** Uncropped Western blot images from four independent experiments probing for total STAT2. **c,** Uncropped Western blot images from four independent experiments probing for loading control GAPDH. HPCs were treated with 1 ng/ml TNF-α for 1, 3, 6, or 12 hours. Molecular weight markers (Precision Plus Protein Kaleidoscope Prestained Protein Standards) are shown for reference. Red arrows indicate the band of interest.

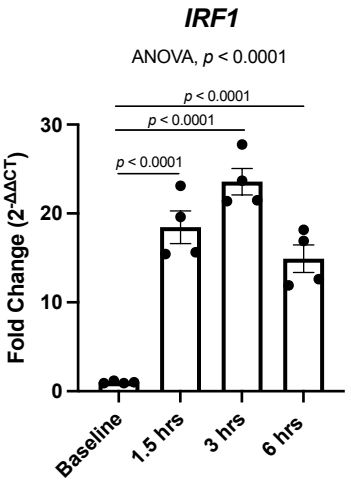

Supplementary Fig. 13 | HPCs upregulate transcription factor *IRF1* in response to TNF-α. RT-qPCR data showing relative *IRF1* gene expression in HPCs treated ± 1 ng/ml TNF-α for 1.5, 3, or 6 hours. Data is presented as mean ± SEM from four independent experiments. Statistical analysis: one-way ANOVA followed by Bonferroni's multiple comparisons test.

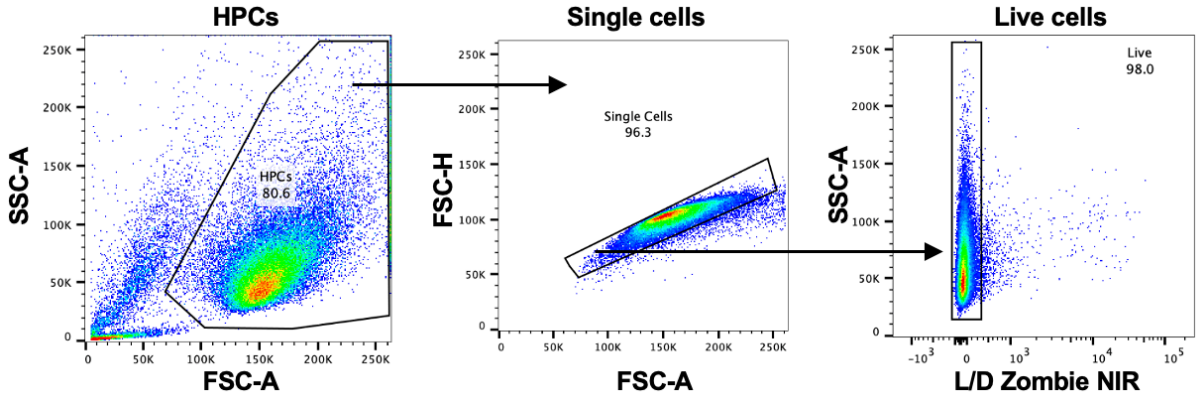

Supplementary Fig. 14 | Gating strategy for assessing cell surface expression on HPCs. Representative gating strategy for analysing cell surface protein expression on live, single HPCs. Cells were first gated based on forward scatter (FSC) and side scatter (SSC) to exclude debris and identify the main population. Singlets were selected using FSC-A versus FSC-H to

exclude doublets. Live cells were identified by negative selection using the Zombie NIR viability dye.

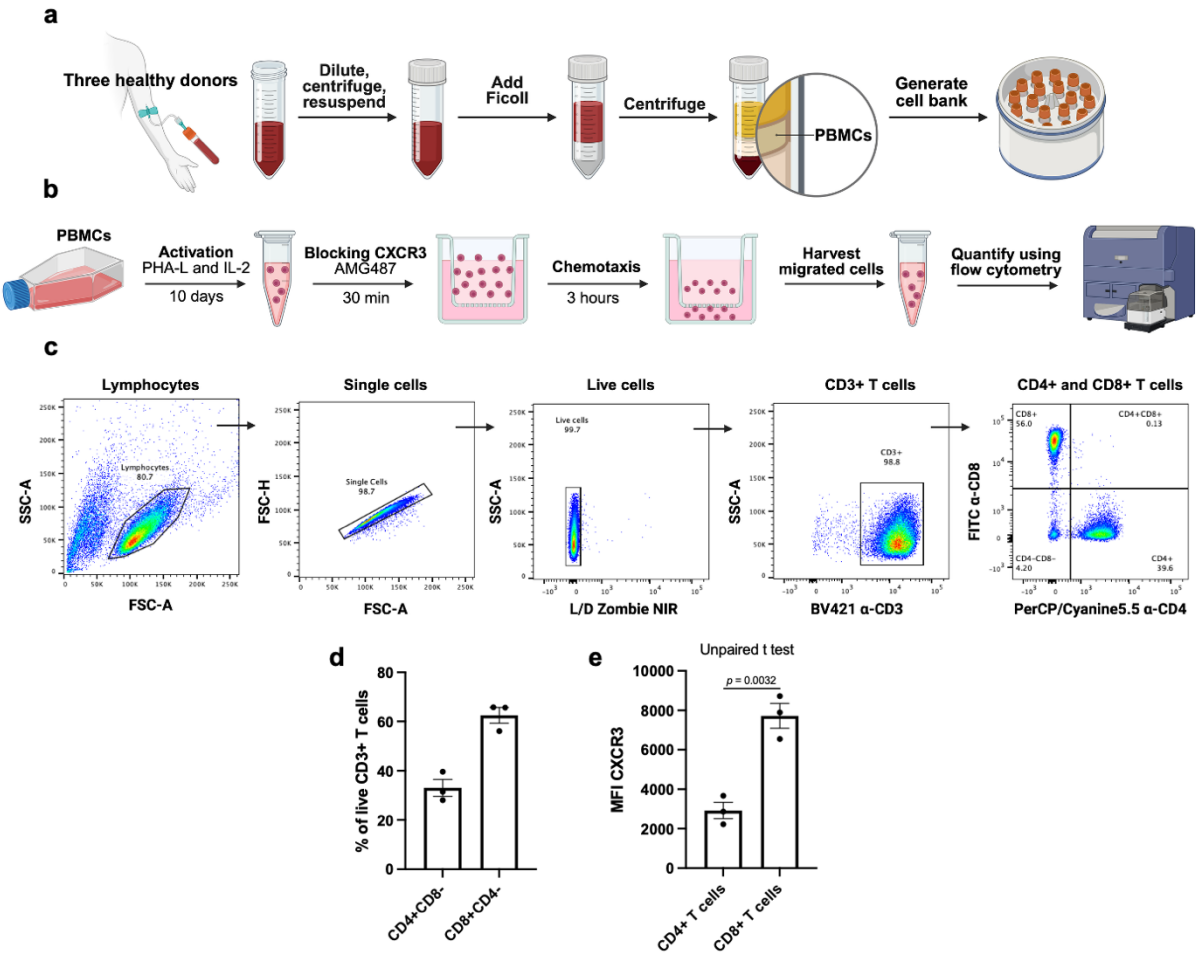

Supplementary Fig. 15 | Transwell chemotaxis assay using primary human T cells to study CXCR3-dependent migration. a, PBMS were isolated from leukocytes cones from three healthy donors using a Ficoll-Paque density gradient, and a cell bank was generated for each donor. **b,** Schematic overview of the T cell chemotaxis assay. **c,** Representative gating strategy to identify CD4+ and CD8+ T cells. **d,** Percentage of T cell subsets following the activation protocol. Data is presented as mean ± SEM from three healthy donors. **e,** Quantification of CXCR3 MFI (median) between CD4+ T cells and CD8+ T cells. Data is presented as mean ± SEM from three healthy donors. Statistical analysis: unpaired, two-tailed, parametric t-test.

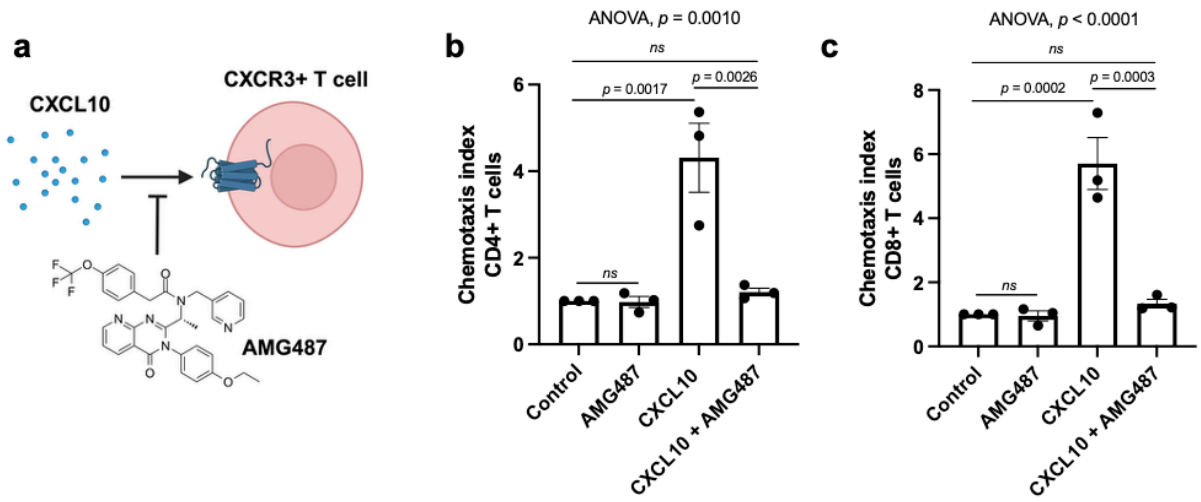

Supplementary Fig. 16 | Recombinant CXCL10 promotes CXCR3-dependent T cell recruitment. a, CXCL10 drives T cell chemotaxis by activating CXCR3. AMG487 is a selective CXCR3 antagonist. **b**, and **c**, Quantification of the chemotactic response (chemotaxis index) of **b** CD4+ T cells and **c** CD8+ T cells treated ± 1 μM AMG487 or DMSO in response to control media or media containing 100 ng/ml recombinant hCXCL10. The chemotactic index is the ratio of the number of cells migrated in response to a stimulus, as compared with controls. Data is represented as mean ± SEM of three healthy donors. Statistical analysis: one-way ANOVA followed by Bonferroni's multiple comparisons test.

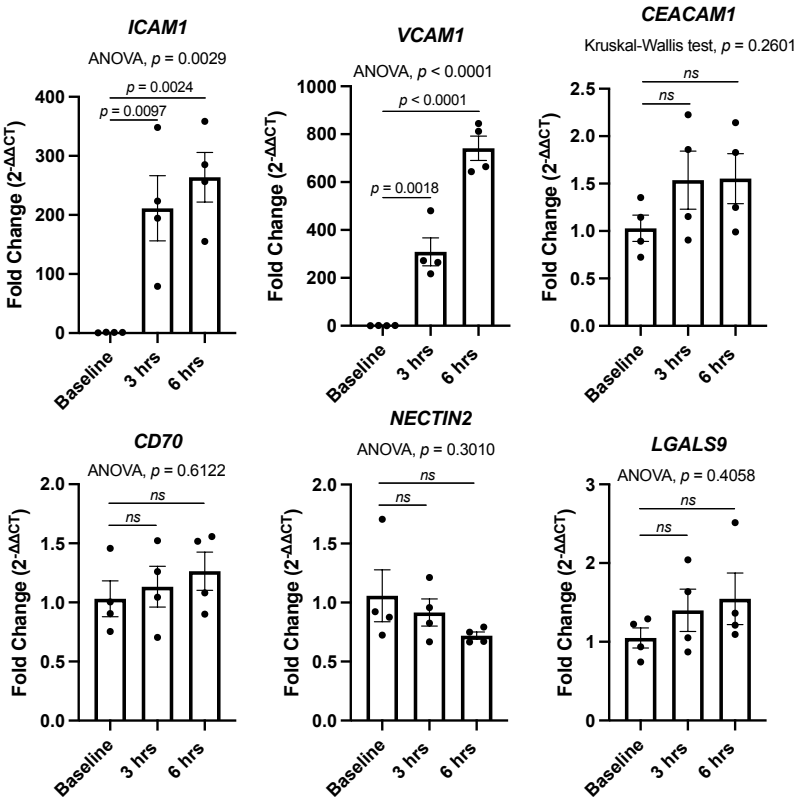

Supplementary Fig. 17 | HPCs upregulate molecules involved in T cell crosstalk in response to TNF-α. RT-qPCR data showing relative gene expression of *ICAM1, VCAM1, CEACAM1, CD70, NECTIN2, and LGALS9* in HPCs treated ± 1 ng/ml TNF-α for 1.5, 3, or 6 hours. Data is presented as mean ± SEM of four independent experiments. Statistical analysis: one-way ANOVA followed by Bonferroni's multiple comparisons test or Kruskal-Wallis test followed by Dunn's post hoc correction as indicated.

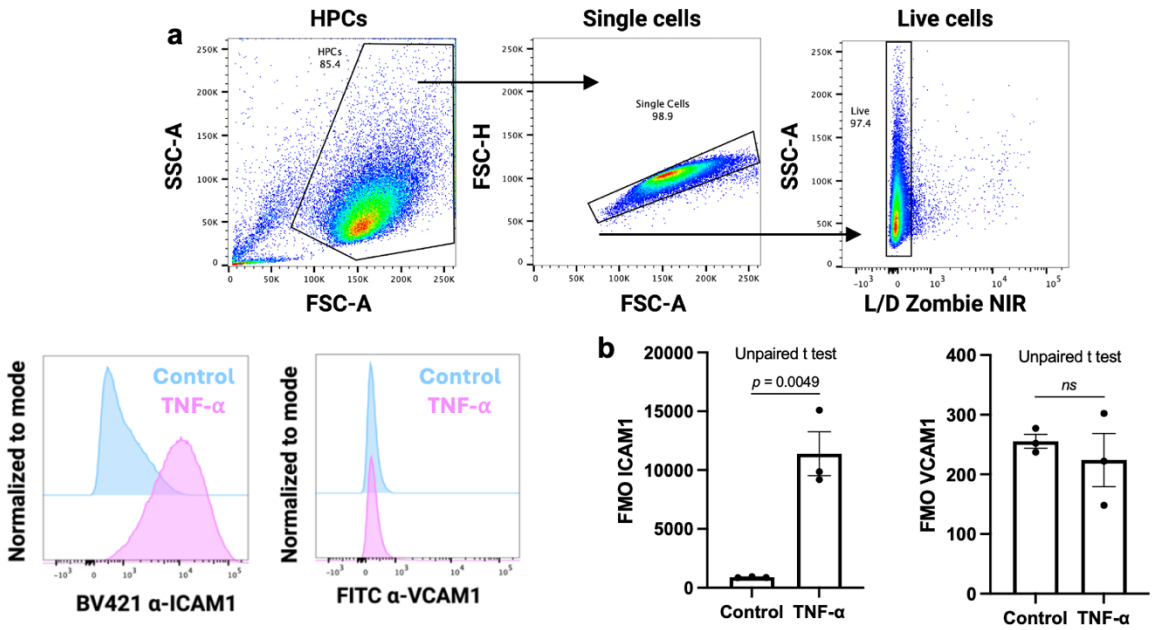

Supplementary Fig. 18 | Cell surface expression of ICAM1 and VCAM1 on HPCs in response to TNF-α. a, Gating strategy for assessing cell surface protein expression on live, single HPCs. Cells were first gated by forward scatter (FSC) and side scatter (SSC) to exclude debris and identify the main population. Singlets were selected using FSC-A versus FSC-H, and live cells were identified by negative selection using the Zombie NIR viability dye. Representative histograms show ICAM1 and VCAM1 on the control-treated (blue) and TNF-α-treated (pink) HPCs. **b**, Quantification of ICAM1 and VCAM1 surface expression by mean fluorescence intensity (MFI) on HPCs treated ± 1 ng/ml TNF-α for 24 h, measured by flow cytometry. Data is presented as mean ± SEM. Statistical analysis: two-tailed, unpaired t test.

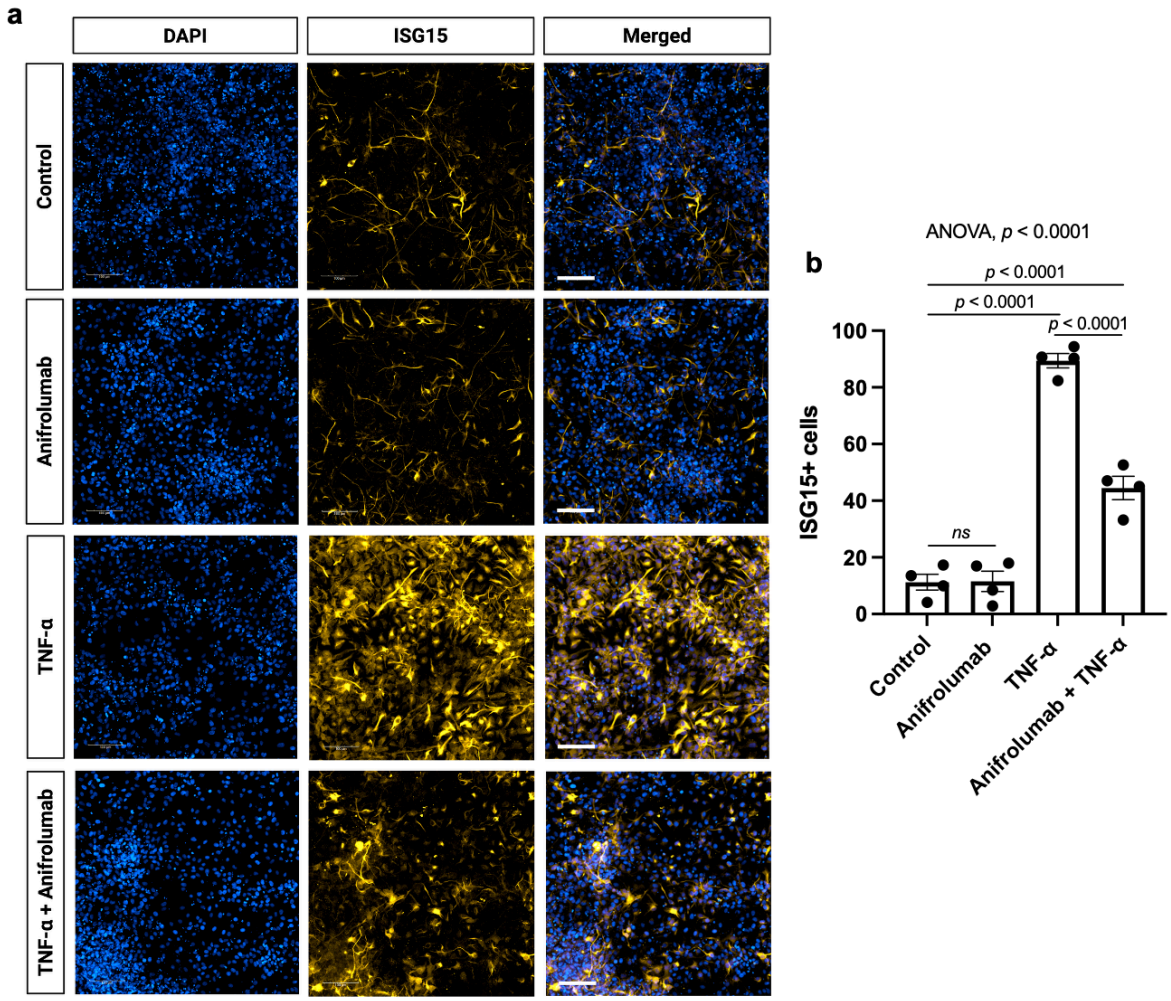

Supplementary Fig. 19 | Blocking IFNAR decreases the upregulation of ISG15+ differentiating HPCs in response to chronic TNF-α. a, Representative images showing the expression of ISG15 (orange) in HPCs differentiated for seven days treated chronically with ± 1 ng/ml TNF-α ± 10 μg/ml anifrolumab. Scale bar, 100 μm. **b,** Quantification of the percentage of ISG15+ cells based on panel **a**. Data represent mean ± SEM from four independent experiments. Statistical analysis: one-way ANOVA followed by Bonferroni's multiple comparisons test.

Antibody	Manufacturer	Catalogue number	Dilution
Mouse Nestin	Chemicon	Mab5326	1:1000
Mouse MAP2	Abcam	Ab11267	1:500
Rabbit DCX	Abcam	Ab18723	1:500
Mouse STAT1	Cell Signalling Technology	9176	1:1000
Rabbit ISG15	Proteintech	15981-1-AP	1:500
Mouse NF-κB p65	Santa Cruz	Sc-8008	1:500

Donkey anti-rabbit Alexa fluor 555	Invitrogen	A-31571	1:500
Donkey anti-rabbit Alexa fluor 488	Invitrogen	A-21202	1:500

Supplementary Table 1 | Primary and secondary antibodies used for immunocytochemistry

Step	Temperature (°C)	Time (minutes)
1	25	10
2	37	120
3	85	5
4	4	∞

Supplementary Table 2 | Thermal cycler program employed for cDNA synthesis

Step	Temperature (°C)	Time
1	50	2 minutes
2	95	10 minutes
3 (40 cycles)	95	15 seconds
4 (40 cycles)	60	1 minute
5	95	15 seconds

Supplementary Table 3 | Thermal cycling conditions employed for RT-qPCR

Gene	Sequence
CD70	Forward: 5'-TTCGCACAGGCTCAGCAGCAG-3' Reverse: 5'-TTGTCCAGCTCTGGTCCATGCA-3'
CEACAM1	Forward: 5'-CACGCCAATAACTCAGTCACTGG-3' Reverse: 5'-TTGTGGAGCAGGTCAGGTTCAC-3'
CXCL10	Forward: 5'-GGTGAGAAGAGATGTCTGAATCC-3' Reverse: 5'-GTCCATCCTTGGAAGCACTGCA-3'
GAPDH	Forward: 5'-GTCTCCTCTGACTTCAACAGCG-3' Reverse: 5'-ACCACCCTGTTGCTGTAGCCAA-3'
ICAM1	Forward: 5'-AGCGGCTGACGTGTGCAGTAAT-3' Reverse: 5'-TCTGAGACCTCTGGCTTCGTCA-3'
IFNB1	Forward: 5'-CTTGGATTCCTACAAAGAAGCAGC-3' Reverse: 5'-TCCTCCTTCTGGAACTGCTGCA-3'
IRF1	Forward: 5'-GAGGAGGTGAAAGACCAGAGCA-3' Reverse: 5'-TAGCATCTCGGCTGGACTTCGA-3'
LGALS9	Forward: 5'-ACACCCAGATCGACAACTCCTG-3' Reverse: 5'-CAAACAGGTGCTGACCATCCAC-3'
NECTIN2	Forward: 5'-GAGCAGATGGTGTCACGGTCAC-3' Reverse: 5'-GAGATGGACACTTCAGGAGGGT-3'
VCAM1	Forward: 5'-GATTCTGTGCCCACAGTAAGGC-3' Reverse: 5'-TGGTCACAGAGCCACCTTCTTG-3'

Supplementary Table 4 | Primers used for RT-qPCR

Target	Company	Catalogue number	Species	Dilution
p-STAT1	Cell Signalling Technology	91715	Rabbit	1:1000
p-STAT2	Cell Signalling Technology	88410	Rabbit	1:1000
GAPDH	Proteintech	60004-1-1g	Mouse	1:10000
STAT1	Cell Signalling Technology	9176	Mouse	1:1000
STAT2	Cell Signalling Technology	71604	Rabbit	1:1000
Anti-rabbit	GE	NA9340V	Donkey	1:3000
Anti-mouse	Santa Cruz Biotechnology	D1321	Goat	1:9000

Supplementary Table 5 | Antibodies used for western blot experiments

Chemokine	Full name	Alias
CCL2	Chemokine (CC motif) ligand 2	MCP-1
CCL3	Chemokine (CC motif) ligand 3	MIP-1α
CCL4	Chemokine (CC motif) ligand 4	MIP-1β
CXCL1	Chemokine (CXC motif) ligand 1	GROα
CXCL5	Chemokine (CXC motif) ligand 5	ENA-78
CXCL8	Chemokine (CXC motif) ligand 8	IL-8
CXCL9	Chemokine (CXC motif) ligand 9	MIG
CXCL10	Chemokine (CXC motif) ligand 10	IP-10
CXCL11	Chemokine (CXC motif) ligand 11	I-TAC
CCL11	Chemokine (CC motif) ligand 11	Eotaxin
CCL17	Chemokine (CC motif) ligand 17	TARC
CCL20	Chemokine (CC motif) ligand 20	MIP-3α

Supplementary Table 6 | Chemokines included in the human pro-inflammatory chemokine panel

Protein	Fluorophore	Company	Catalogue number	Dilution
ICAM1	BV421	Biolegend	353132	1:100
VCAM1	FITC	R&D	BBA22	1:100
Tetherin (BST2)	APC	Biolegend	348410	1:100

Supplementary Table 7 | Antibodies used to analyse cell surface protein expression on HPCs

Protein	Fluorophore	Company	Catalogue number	Dilution
CXCR3	PE	Biolegend	353706	1:100
CD3	BV421	Biolegend	317344	1:100
CD4	PerCP/Cyanine5.5	Biolegend	317428	1:100
CD8	FITC	Biolegend	980908	1:100

Supplementary Table 8 | Antibodies used to analyse cell surface protein expression on immune cells